Scatter-Free Infrared Spectra of Single, Isolated 5 μm Particles of Respirable Dust

A Senior Honors Thesis

Presented in Partial Fulfillment of the Requirements of the *graduation with research distinction* in Chemistry in the undergraduate colleges of The Ohio State University

By
Matthew C. McCormack
Undergraduate Honors Thesis Program in Chemistry

The Ohio State University
2010

Honors Thesis Committee: Dr. Eric Herbst, Dr. Kristin Sellgren
Project Advisor: Professor James V. Coe, Department of Chemistry

Copyright by

Matthew C. McCormack

2010

ABSTRACT

The phenomenon of extraordinary transmission on subwavelength metal mesh arrays, as assisted by propagating surface plasmons (PSPs), will be used to obtain essentially scatter-free infrared spectra of individual dust particles that fill the holes of the mesh. This technique allows for the characterization and quantification of the materials in the dust with an emphasis on single, isolated particles in the respirable size range, specifically 1-5 μm. With the combined use of a variety of instruments including the Scanning Electron Microscope (SEM), Optical Microscope, and IR imaging microscope, the physical characterization of the dust particles will be analyzed. Calibration spectra of known materials were also obtained, including calcite, dolomite, gypsum, quartz, and kaolinite. Once the IR spectrum of the individual particles is obtained, Mie Scattering Theory and Bruggeman Effective Medium Theory are used to model the individual particle spectra and begin to characterize and quantify the chemical components of the individual particles.

VITA

2003- 2006 .....Edgewood Senior High School

Ashtabula, OH

2006 to present .....B.S. Chemistry, Department of Chemistry

The Ohio State University

FIELDS OF STUDY

Major Field: Chemistry

ACKNOWLEDGMENTS

I would like to thank Dr. Coe and my fellow group members for all of the knowledge they have shared with me throughout our experiences together. It will stay with me for the rest of my life.

TABLE OF CONTENTS

LIST OF FIGURES

LIST OF TABLES

CHAPTER 1
INTRODUCTION

1.1 WHY IS DUST IMPORTANT?

Dust, however small and seemingly insignificant, plays an integral part in our daily lives. The general definition of dust is solid particles with diameters less than 500 μm. Particulate matter has a wide variety of sources from human skin and hair, dirt lifted by the wind, mountainous materials, volcanic eruptions, and pollution[1]. The effects of dust are especially important for people with diseases such as asthma, hay fever, and other respiratory illnesses. However everyone is affected by dust, and inhaling large quantities of particulate matter can be detrimental to one's overall health[1-5].

Other important sources of dust derive from occupational sources such as from road ways and coal mines[6]. Dust kicked up by vehicles on roads has been found to contribute up to 33% of the overall air pollution and include deposition of vehicle exhausts, tire and brake wear, and dust created by road construction[7]. Coal dust has been found to cause pneumoconiosis, restriction of lung capacity from particulate matter, and black lung. Other occupational risks involving particulate matter include cotton, Masonry, and wood workers. Cotton workers can develop what is known as brown lung, due to the mixture of pollen, dirt, bacteria, and other plant parts in the dust. Masonry workers can be exposed to increased amounts of quartz, a component that is contained in a large portion of the dust particles in this study, and can lead to acute silicosis. Wood workers can suffer from sequoiosis and paper-mill-workers lung. Wood and cotton provide for good surfaces for the accumulation of fungi, bacteria, and viruses which can

then lead to more complex health issues.

Dust storms are one example of a case where exposure to particulate matter could directly affect one's health[4]. Dust storms occur when there is an excess of particulate matter in the air. Due to the increased amount of research and knowledge on the effects of fine particulate matter, the Environmental Protection Agency (EPA) monitors and categorizes the level of dust in the air with a particulate matter, PM, rating and a color ranking system in order to easily communicate the quality of the air to the general public[2]. Dust storms can deposit as much as 1 mm of particulate matter and have a tremendous impact on the visibility, climate, and air quality on places far from the source of the storm[8].

In December of 1952, London experienced a PM_{10} concentration, particles less than 10 μm, to be between 3,000 and 14,000 $\mu g/cm^3$. Normal levels are, on average, 30 $\mu g/cm^3$ and the EPA's "green" level PM_{10} is between 0-54 $\mu g/cm^3$[2]. That year London experienced as much as 12,000 mortalities[3], demonstrating the direct correlation between the amount of dust in the air and health of the general population.

The size range of dust investigated in this study is very important to the body's respiratory system. The body is equipped to deal with small amounts of particulate matter, however, not overexposure. Dust larger than 10 μm is trapped by the nose and throat, and while some of the dust can be expelled through phlegm[9], particles 1-5 μm can enter the deepest parts of the lungs and even into the alveoli. Thus the dust used in this study, has a particular importance as these are the particles that will enter and reside in the lungs[5].

1.2 Purpose of this Study

This increased awareness of the effects of dust and particulate matter on the population has made research, and the providing of additional information on the components of the dust, invaluable. This study provides for a dust calibration model, which includes the major components found in the dust, and through the simulation of the spectra, provides for the quantification of each of these materials in the dust.

CHAPTER 2
COLLECTING DUST ON MESH

2.1 COLLECTING DUST IN THE HOLES OF MESH

Air from room 0055 of Evans Lab, Ohio State University, provided the dust used in this study. Air was drawn through a Quik Start vacuum system for 18 hours at 5 L/min where the dust would collect on a small piece of the metal mesh. Our mesh is a plasmonic film of Ni metal with a square array of holes that are ~5 μm width, 12.6 μm apart from each other, with 2 μm thickness. The mesh was taped over an 1/8" hole in a 25 mm piece of stainless steel shim stock which allowed the mesh and shim stock to directly replace an air filter in a standard size 25 mm in-line Derlin Filter Holder made by SKC Inc. This filter holder has a length of 2 cm, diameter of 3.5 cm, and an effective filtration area of 3.7 cm^2. The dusty mesh was then analyzed under the optical microscope (Olympus B40) with a 50x objective and pictures were captured by a computer to ensure dust has been drawn into the holes of the mesh.

The calibrants used in this dust model were calcite ($CaCO_3$), dolomite $(Mg,Ca)CO_3$, gypsum ($CaSO_4 \cdot 2H_2O$), quartz (SiO_2), and kaolinite ($Al_2Si_2O_5(OH)_4$). Each of the calibration components were ground down with a mortar and pestle, if necessary, and a small amount of the powder was placed on the mesh. It was then placed on the end of a hose attached to a vacuum hose line to maximize the amount of material in the holes while excess material was tapped off to minimize the amount of material on the surface of the mesh.

Figure 2.1 has SEM images of dust on mesh. The sample was gold sputter coated for 40 s.

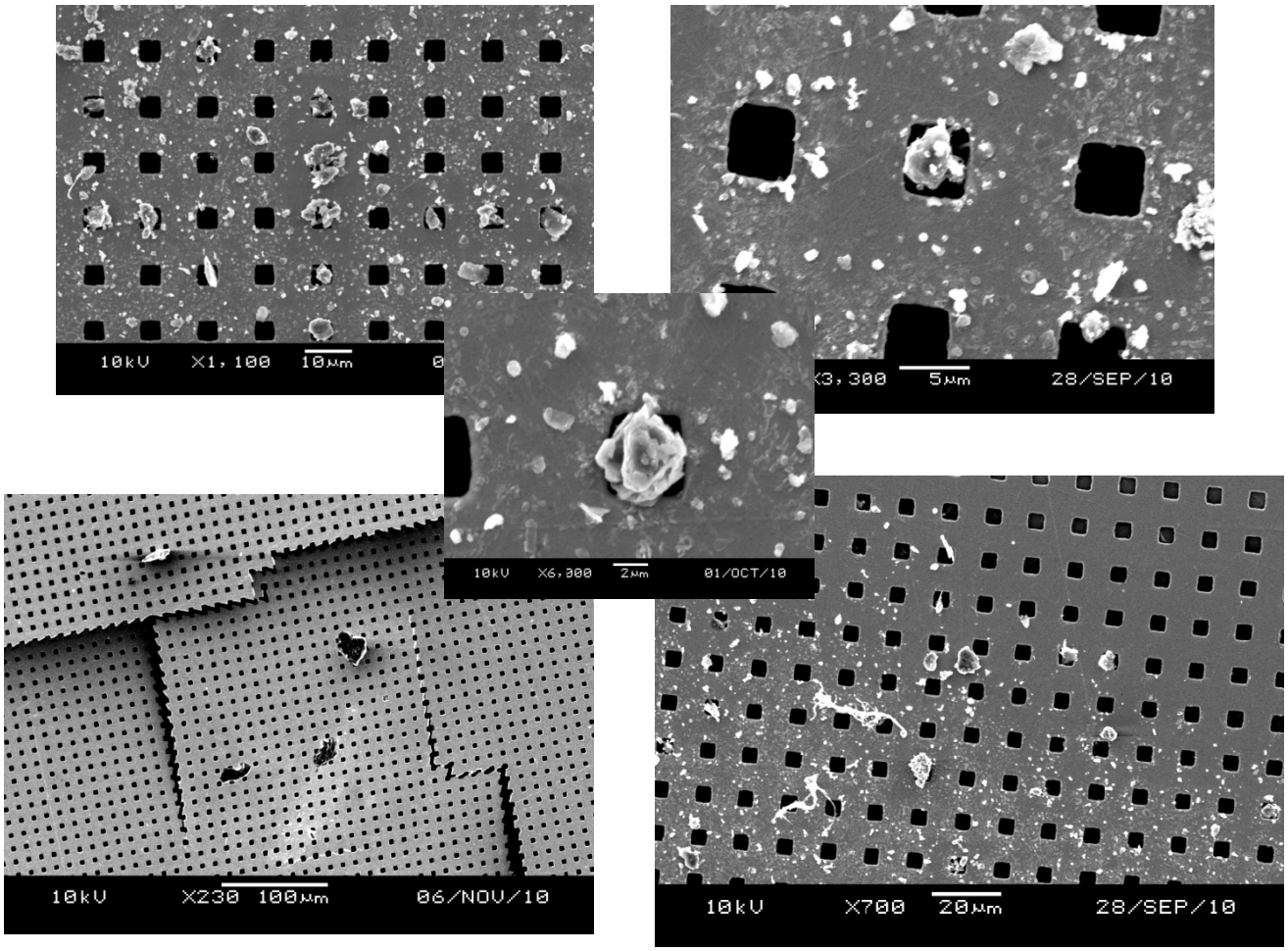

Figure 2.1: SEM Images of dust in the holes of mesh.

CHAPTER 3
INFRARED SPECTRA OF INDIVIDUAL PARTICLES

3.1 Obtaining IR Spectra of Individual Particles

Once the mesh was inspected and confirmed to contain dust in the holes by the Optical Microscope, infrared (IR) spectra of the dusty mesh were recorded with the Perkin Elmer Spectrum Spotlight 300 IR imaging microscope. It is equipped with an array of 16 N_2 (l) cooled Mercury Cadmium Telluride (MCT) detectors. It has an imaging resolution of 6.25 μm and a wavenumber range of 700-7800 cm^{-1}. Light incident on the sample from the Cassegrain optical system comes in a cone with a range of angles from 17º to 37º.

The two types of scans used in this experiment were point mode and image mode scans. All scans were in the range of 700-4000 cm^{-1} with a 4 cm^{-1} resolution. Point mode scans were performed on five 200x200 μm regions of the dusty mesh and averaged to get the "bulk" dust spectra. These take approximately 10 min depending on the size of the scan region. Image mode scans take between 4-6 hours depending on the size and number of IR Images. Image mode scans take IR spectra at every 6.25 μm creating a grid of spectral points that allow for Chemimap/Absorbance Contours to be used to indicate each dust particle in the image by a characteristic vibrational frequency (Fig. 3.1).

Figure 3.1 shows the use of a 3x3 pixel, 18.75x18.75 μm, standard box size that will co-add all spectra at each grid point inside of the box. The same size box is drawn to acquire the background spectra of a region of empty mesh, wherein the particle's spectra can be obtained by ratio to the background transmission spectra.

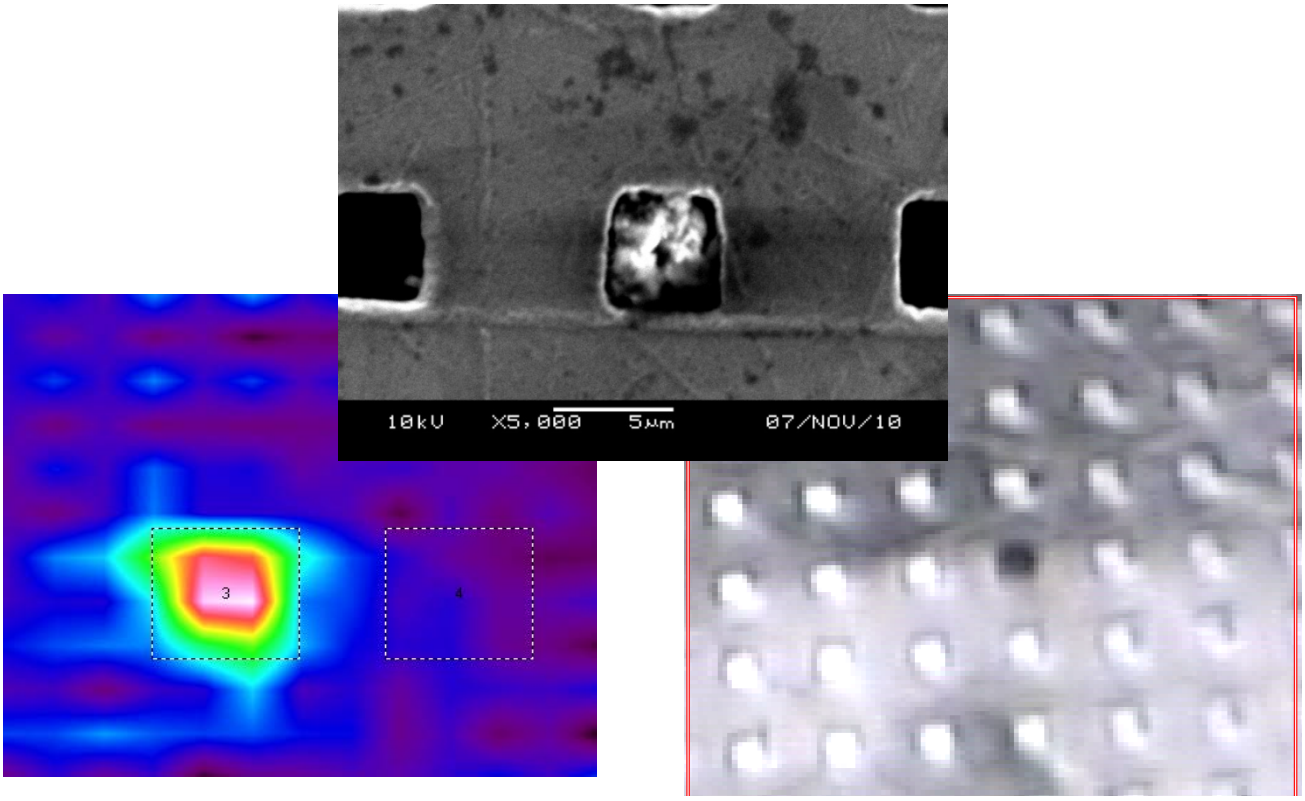

Figure 3.1: Above is an SEM Image of dust particle Abby1. Left is the Absorbance Contour Map of Abby1 isolated from the vibrational frequency at 1031 cm^{-1}. To the right is the corresponding IR Optical Microscope image.

SEM images and the corresponding IR spectra were obtained for two dust particles named “Abby1” and “Abby2.” A characteristic tear in the mesh, as shown in Figure 2.1, allowed for the SEM image and corresponding IR Spectra to be obtained for the same particle. This allowed for the physical characterization of the shape and size, verifying whether it is a collection of smaller particles or a single material. We can then comment on whether its shape, size, or orientation has any effect on the IR spectra.

3.2 X-Ray Fluorescence (XRF) Analysis of Dust

XRF Analysis was used on a sample of dust taken from a bookcase in 0053 EL. XRF spectra were taken with the Innov X XRF Analyzer with a range of 0-20 keV and a scan time of 30 min. The signal of the XRF is not linearly proportional to concentration and more signal arises with heavier elements. The XRF was utilized to help identify the components of the dust and narrow the search for calibration materials. It proved particularly useful in identifying Zn and Fe as two important components in the dust. Their most common oxide species, ZnO and Fe_2O_3, do not have any intense vibrations in the range of our IR spectra and without this analysis, it would be difficult to pick out the small evidence of these species in the IR spectra.

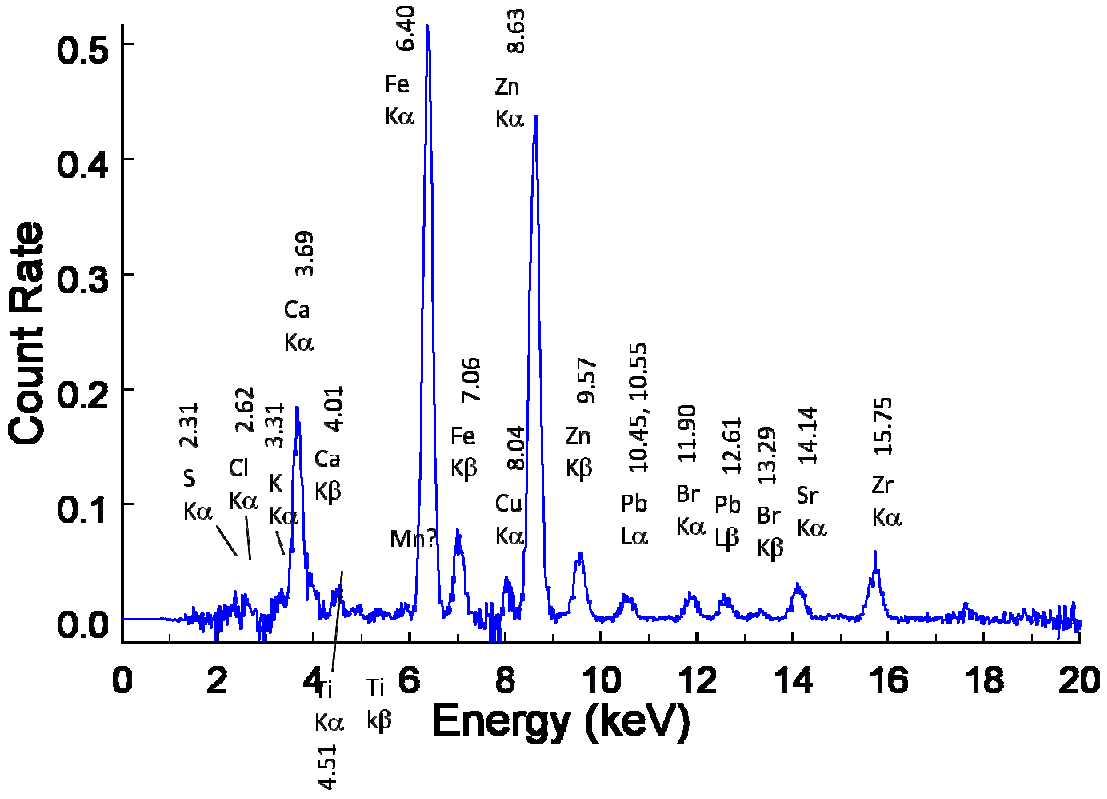

Figure 3.2: XRF Analysis of dust taken from a bookshelf in Evans Lab.

3.3 Point Mode Bulk Spectra vs. Average of 63 Individual Particle Spectra

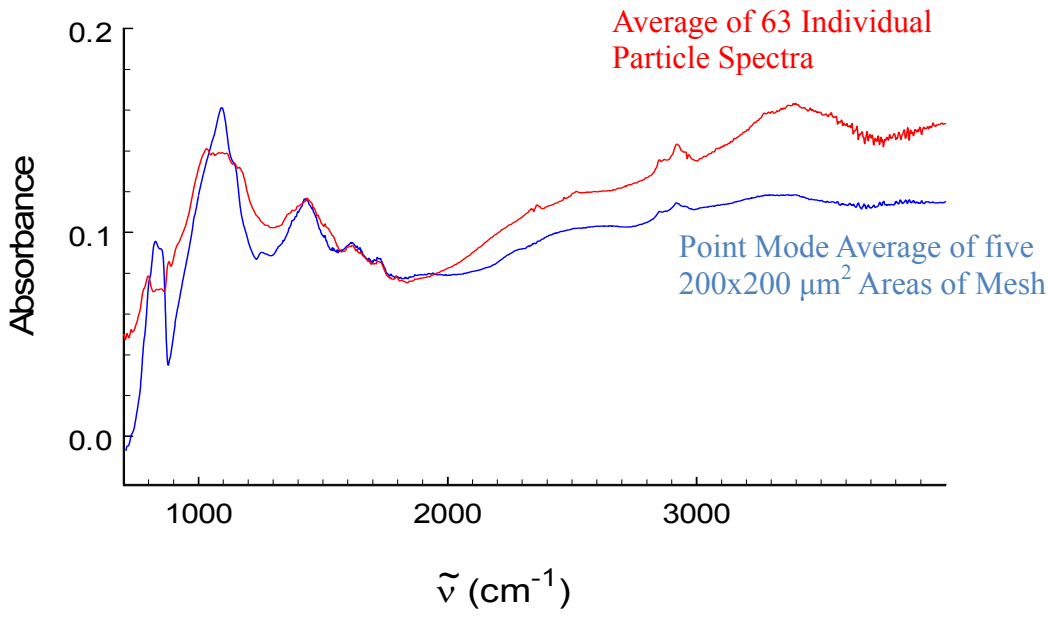

Figure 3.3: Blue curve is the Point Mode average of five 200x200 μm^2 areas of dusty mesh. The red curve is the average of 63 spectra of individual particles from the same mesh sample.

Point mode scans were done on five 200x200 μm^2 dusty regions of mesh and averaged together and then compared to the average of 63 individual particle spectra. Both spectra have a range from 700-4000 cm^{-1}, a resolution of 4 cm^{-1}, and are 512 scans/pixel. The two curves have very similar features. This indicates that the 63 individual particles are a good representation of the dust in the sample.

3.4 Spectra of Individual Particles

All individual particle spectra range from 700-4000 cm^{-1}, have a resolution of 4 cm^{-1}, and are 512 scans/pixel. Images were taken of dusty regions of mesh that contained particles in the holes of the mesh while a blank region of the mesh was used as a background. Each was obtained using the 3x3 pixel box size to correlate with previous work on latex spheres that calibrated the signal from this size image aperture[10].

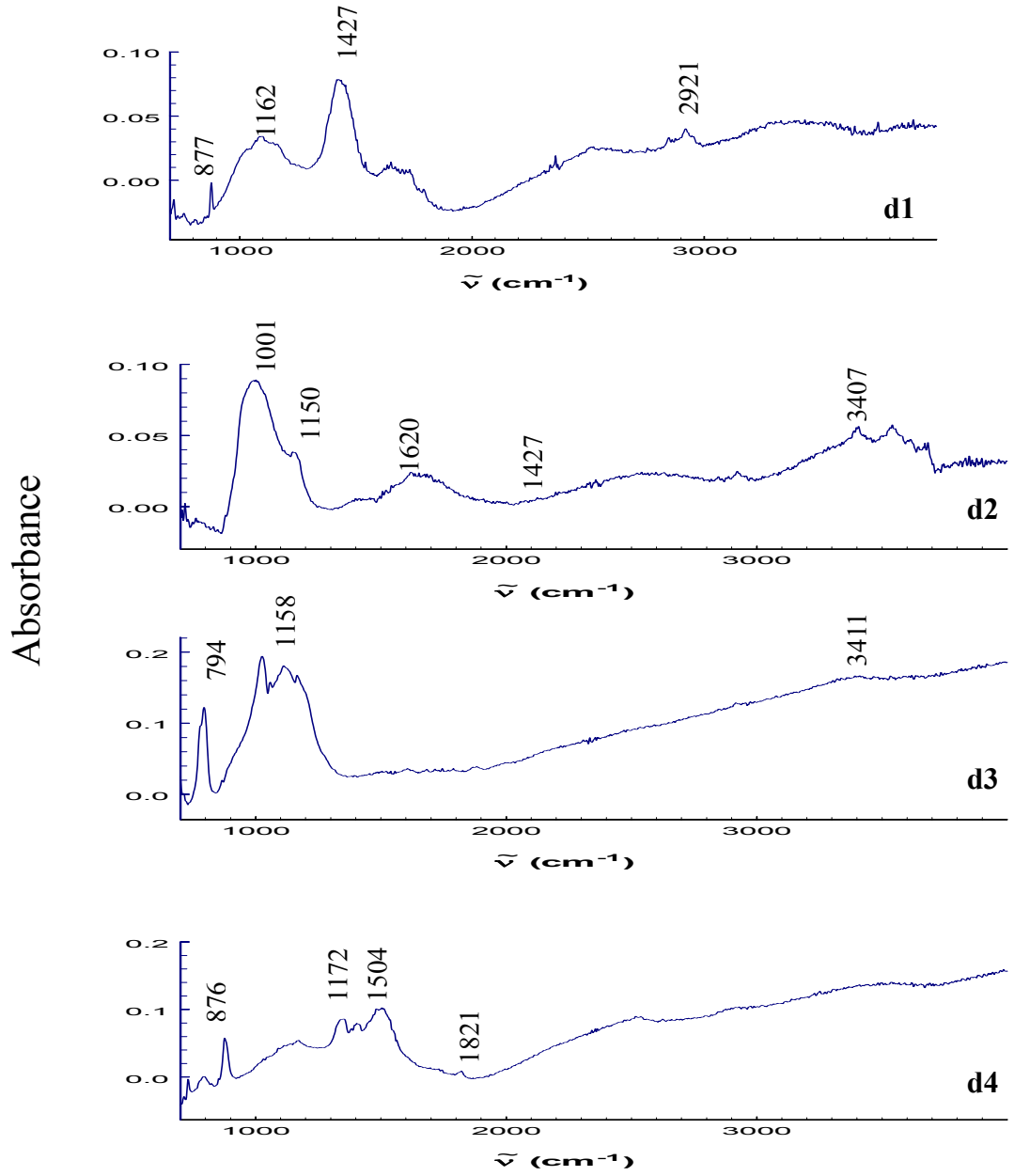

Figure 3.4.1: IR spectra of dust particles d 1, 2, 3, 4.

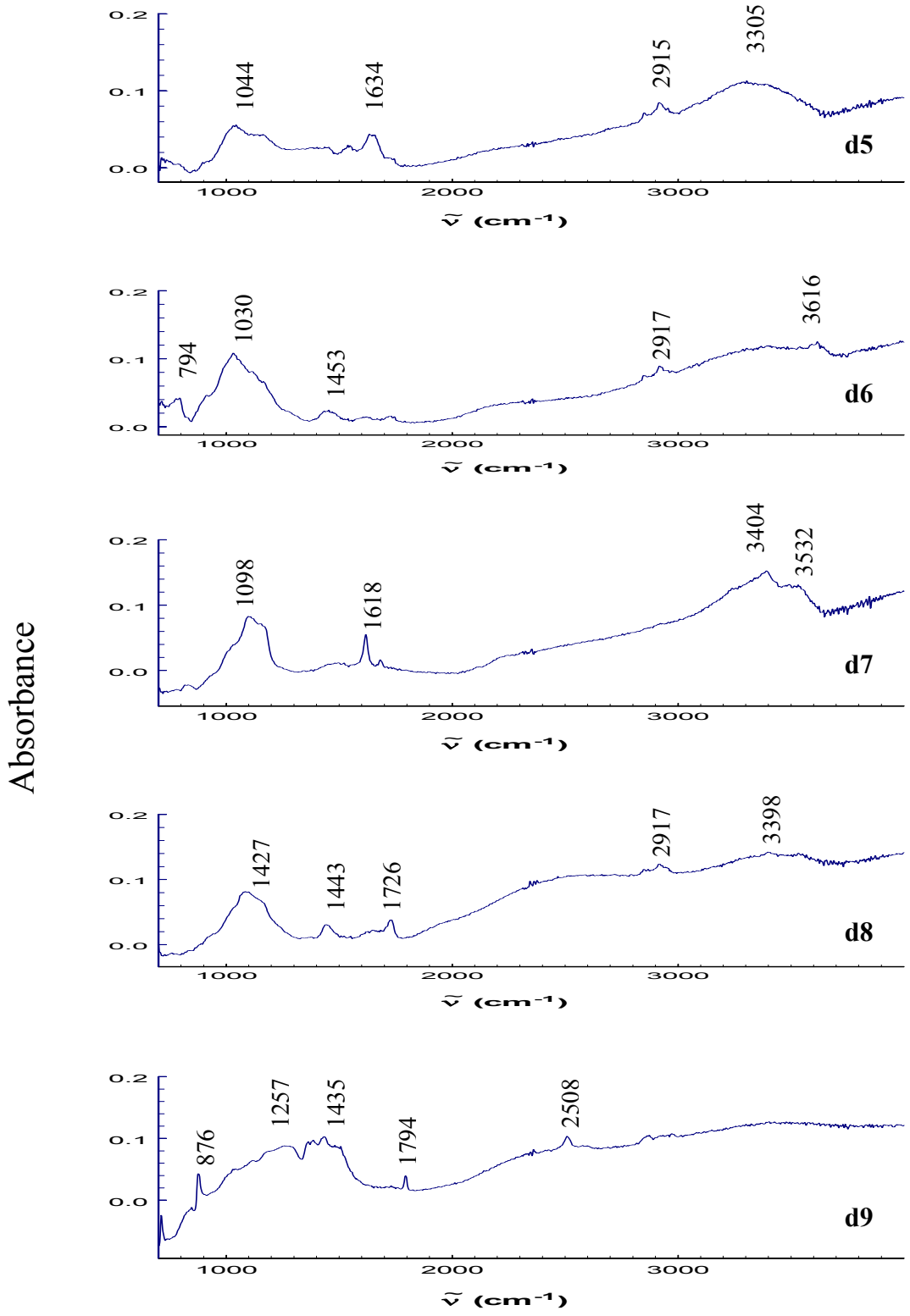

Figure 3.4.2: IR spectra of dust particles d 5, 6, 7, 8, 9.

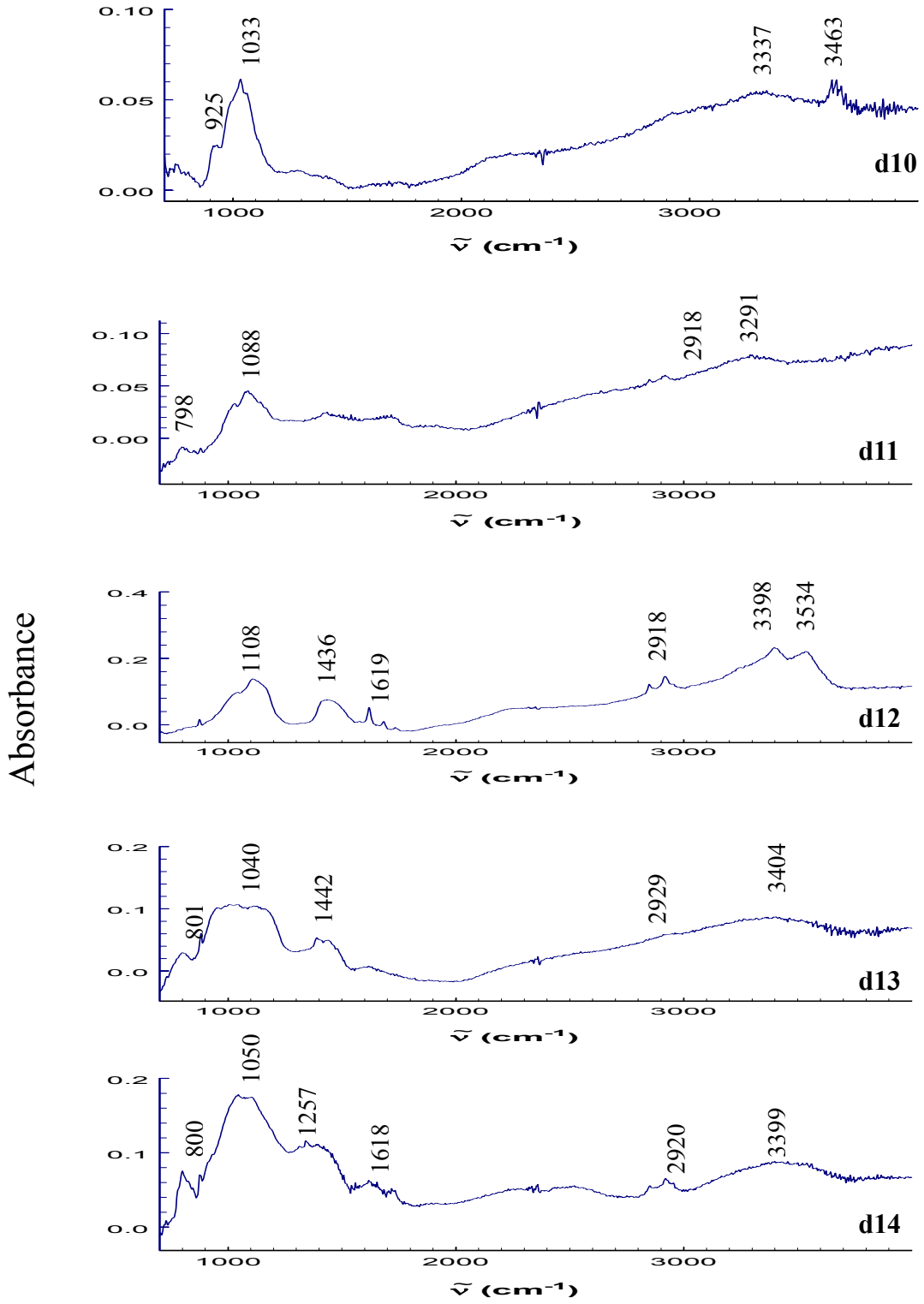

Figure 3.4.3: IR spectra of dust particles d 10, 11, 12, 13, 14.

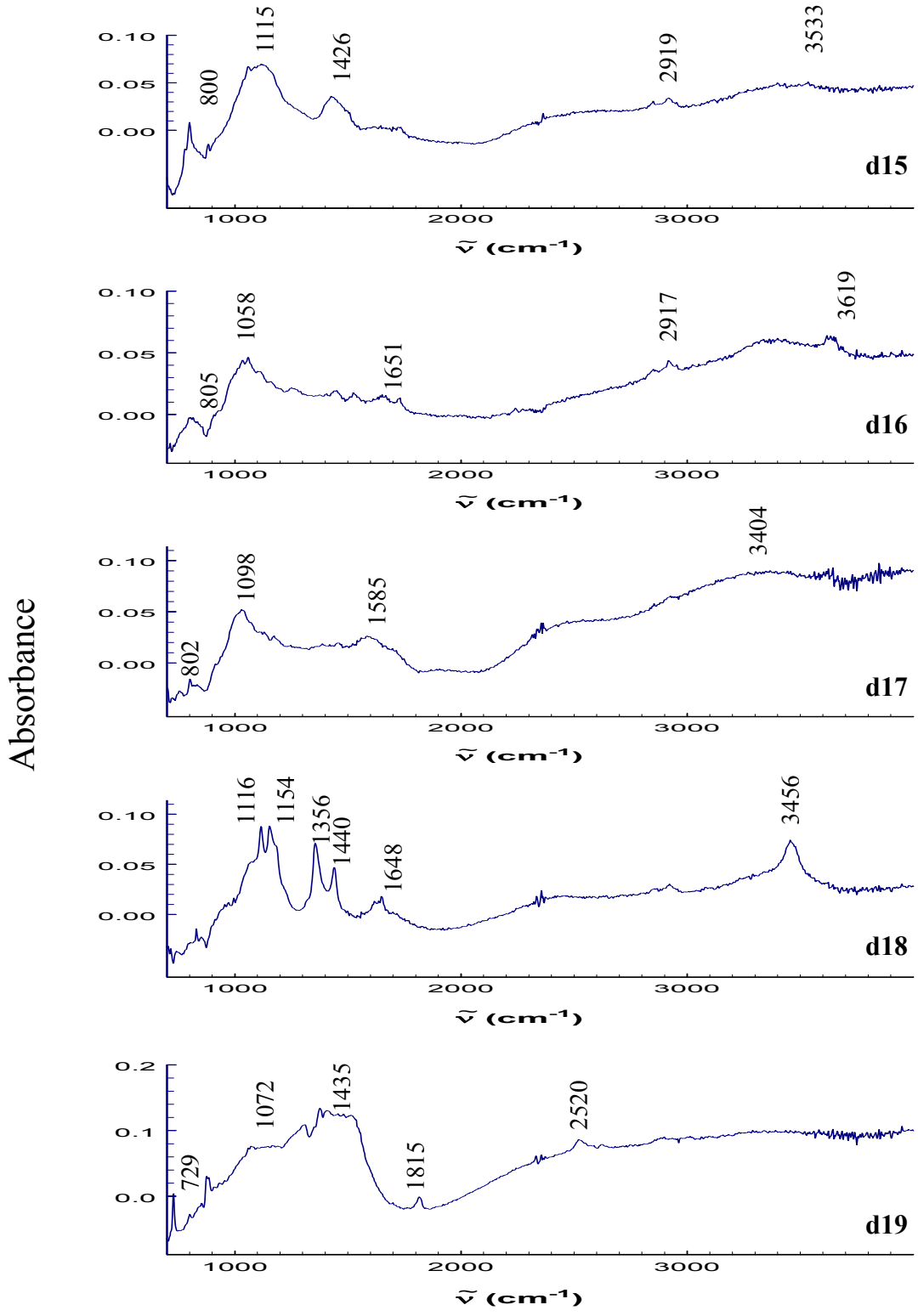

Figure 3.4.4: IR spectra of dust particles d 15, 16, 17, 18, 19.

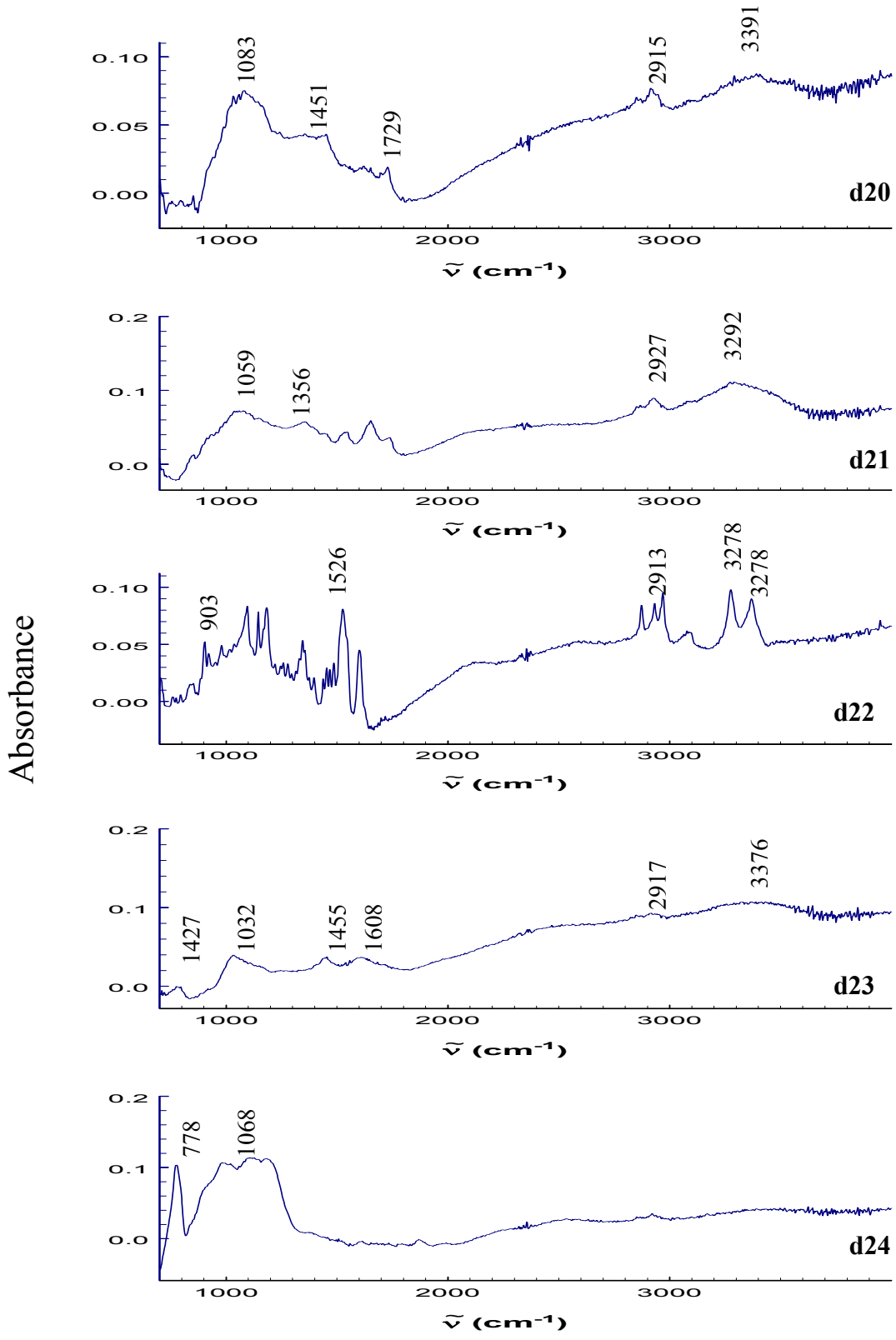

Figure 3.4.5: IR spectra of dust particles d 20, 21, 22, 23, 24.

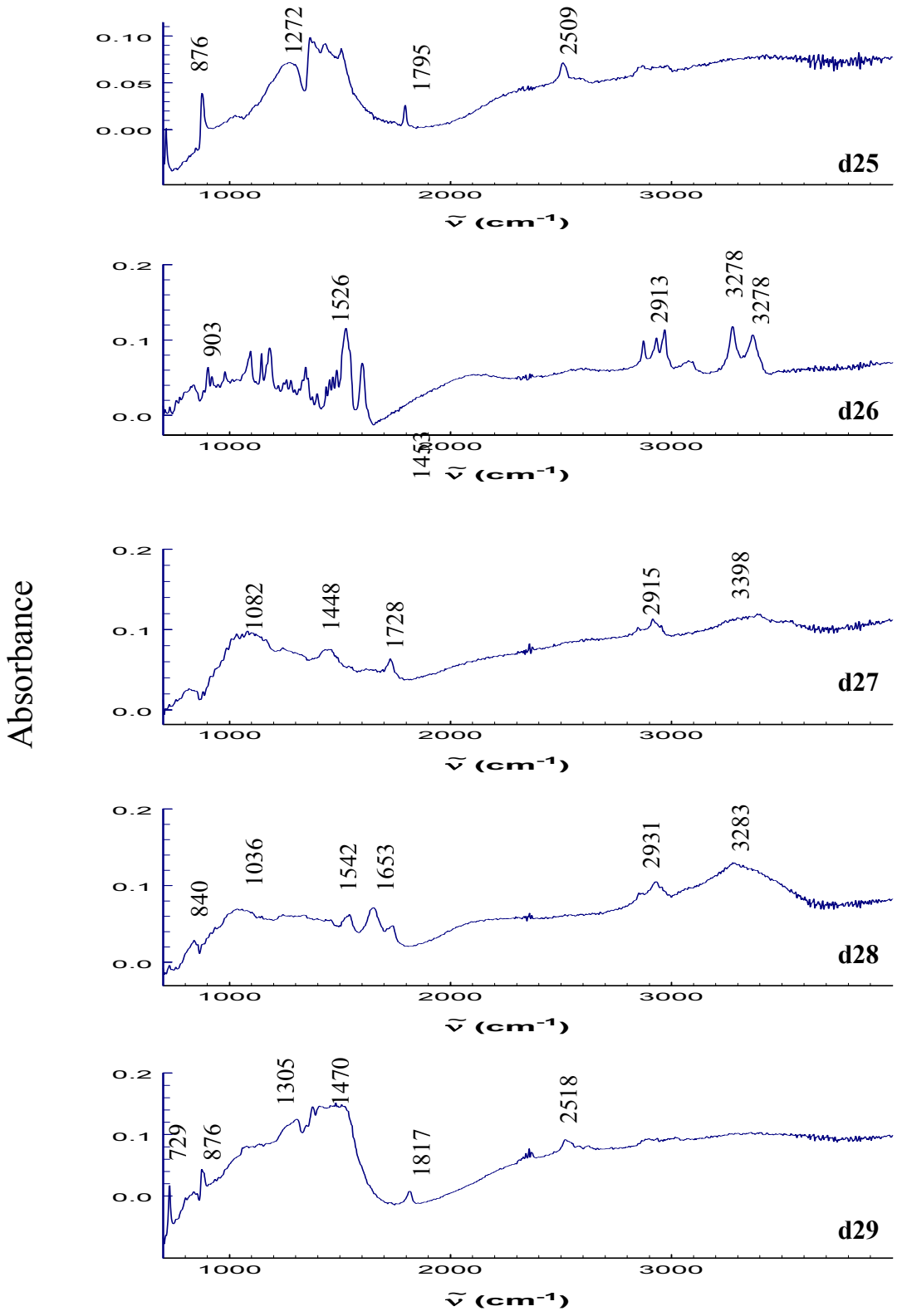

Figure 3.4.6: IR spectra of dust particles d 25, 26, 27, 28, 29.

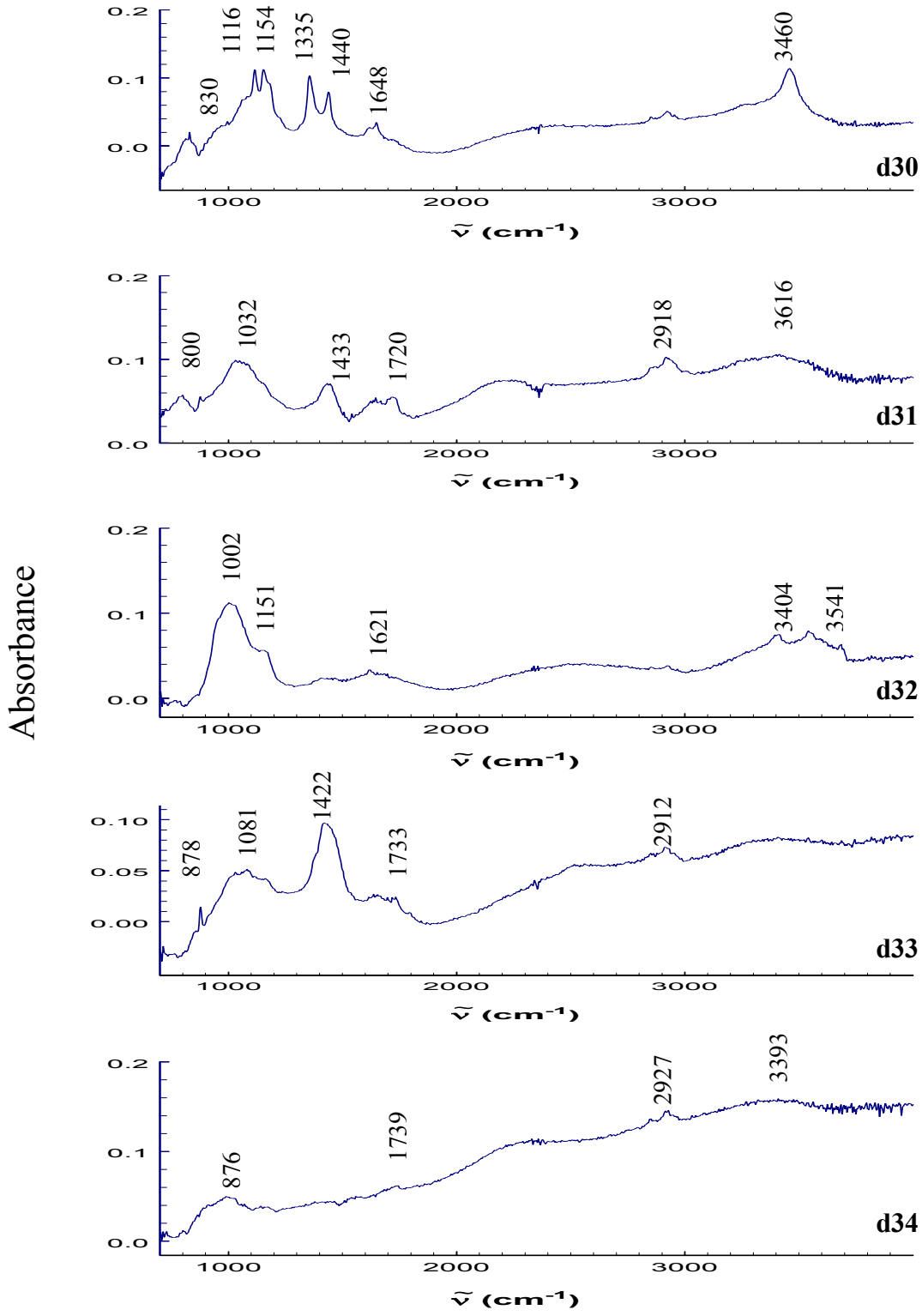

Figure 3.4.7: IR spectra of dust particles d 30, 31, 32, 33, 34.

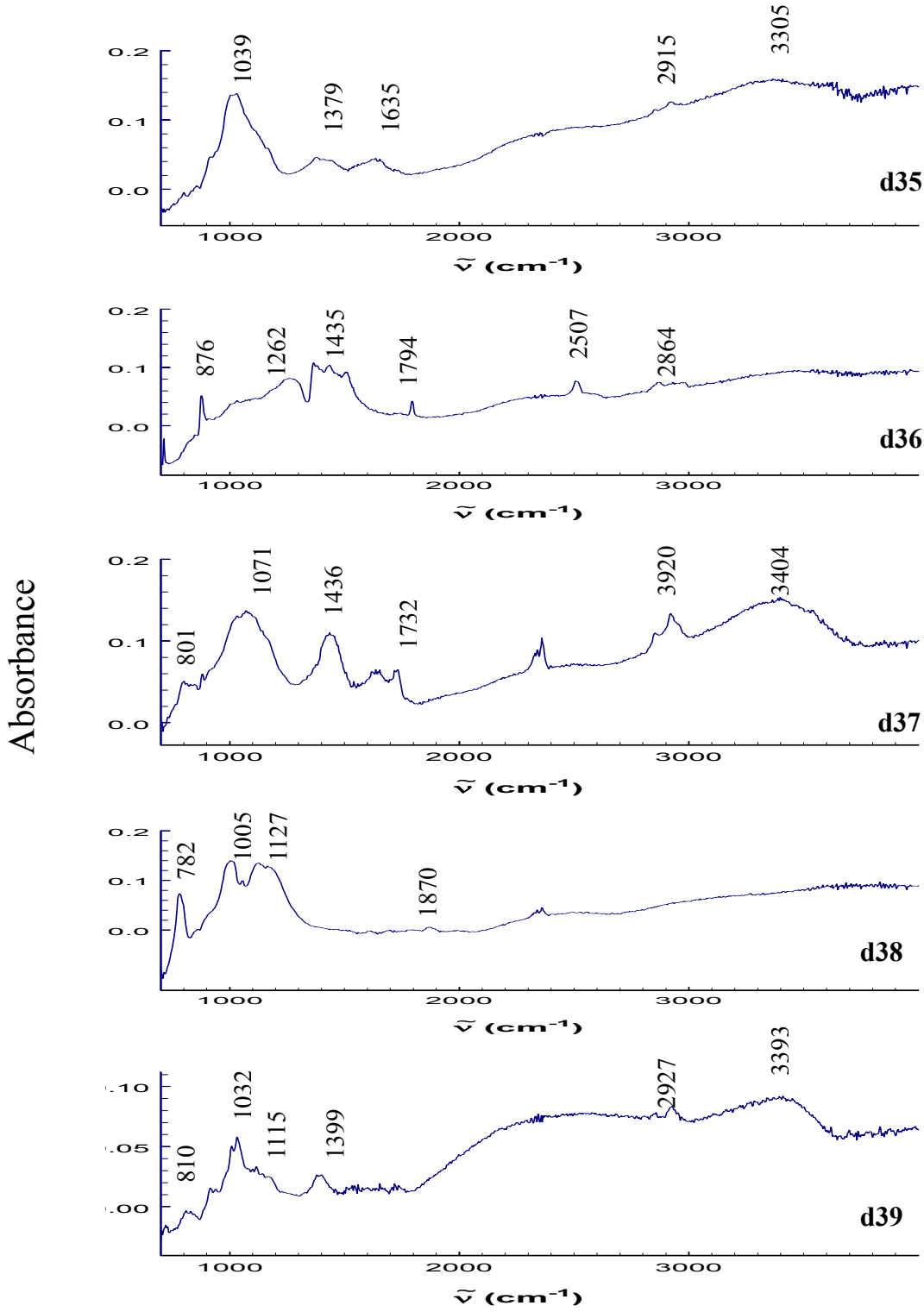

Figure 3.4.8: IR spectra of dust particles d 35, 36, 37, 38, 39.

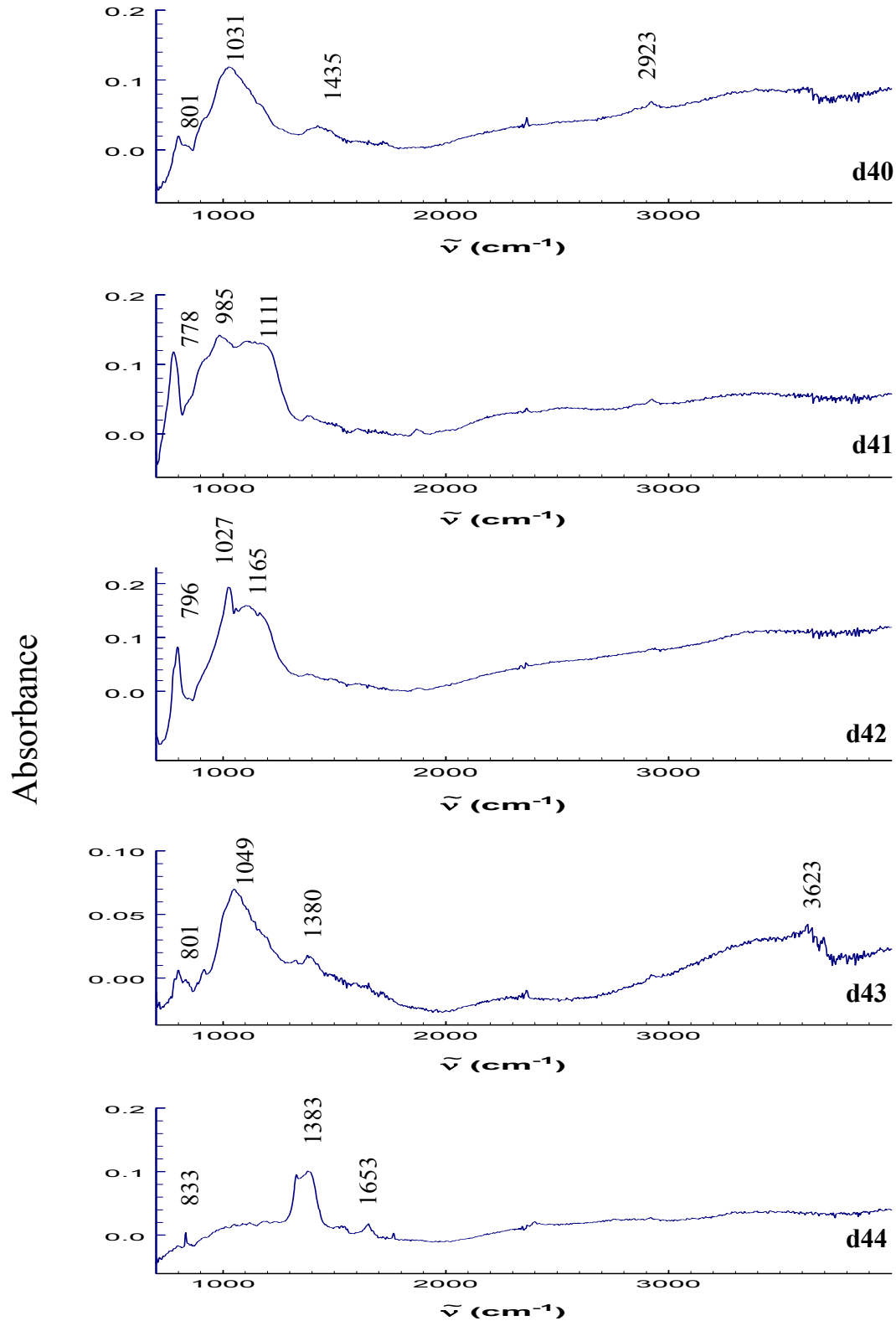

Figure 3.4.9: IR spectra of dust particles d 40, 41, 42, 43, 44.

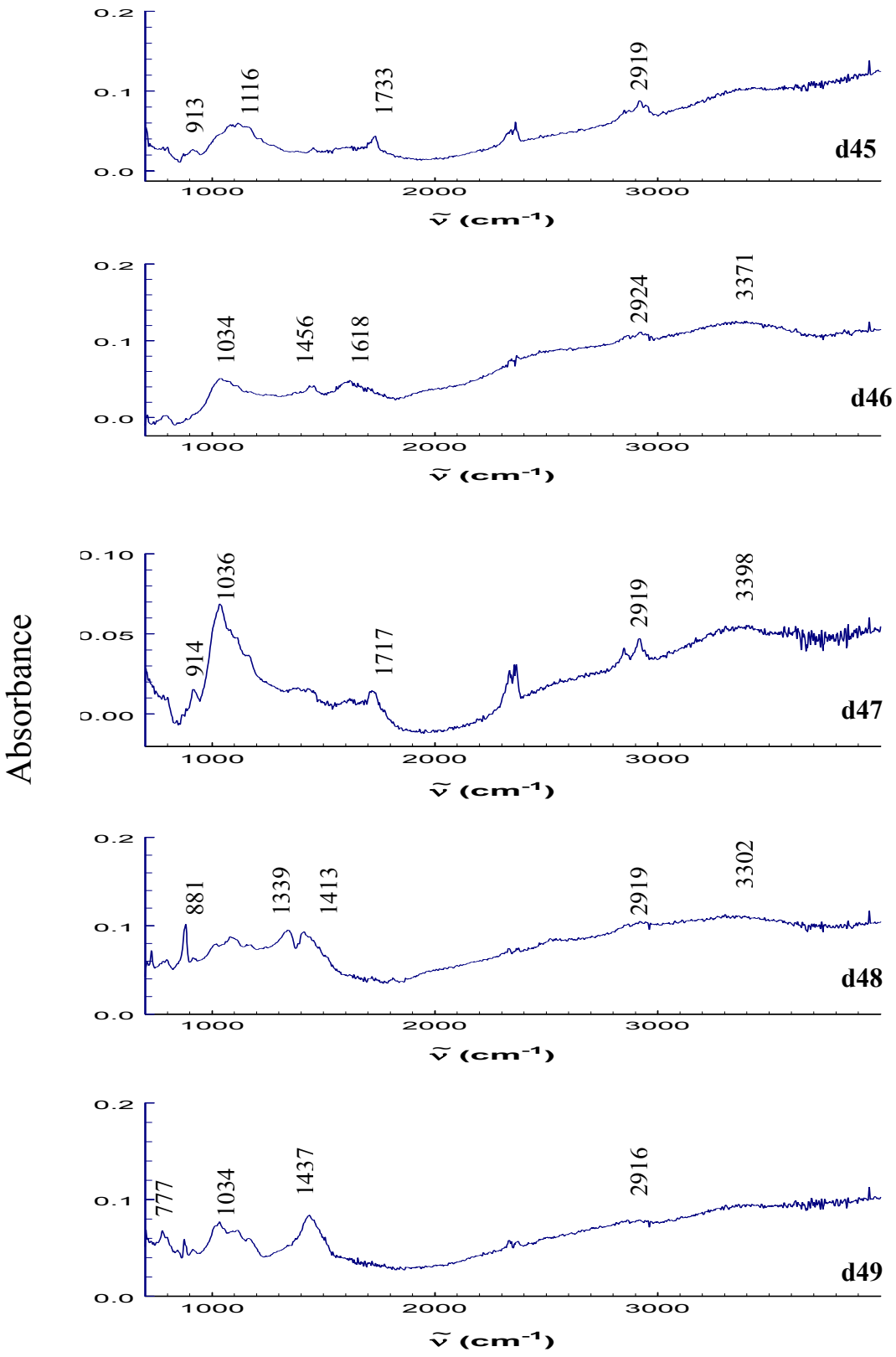

Figure 3.4.10: IR spectra of dust particles d 45, 46, 47, 48, 49.

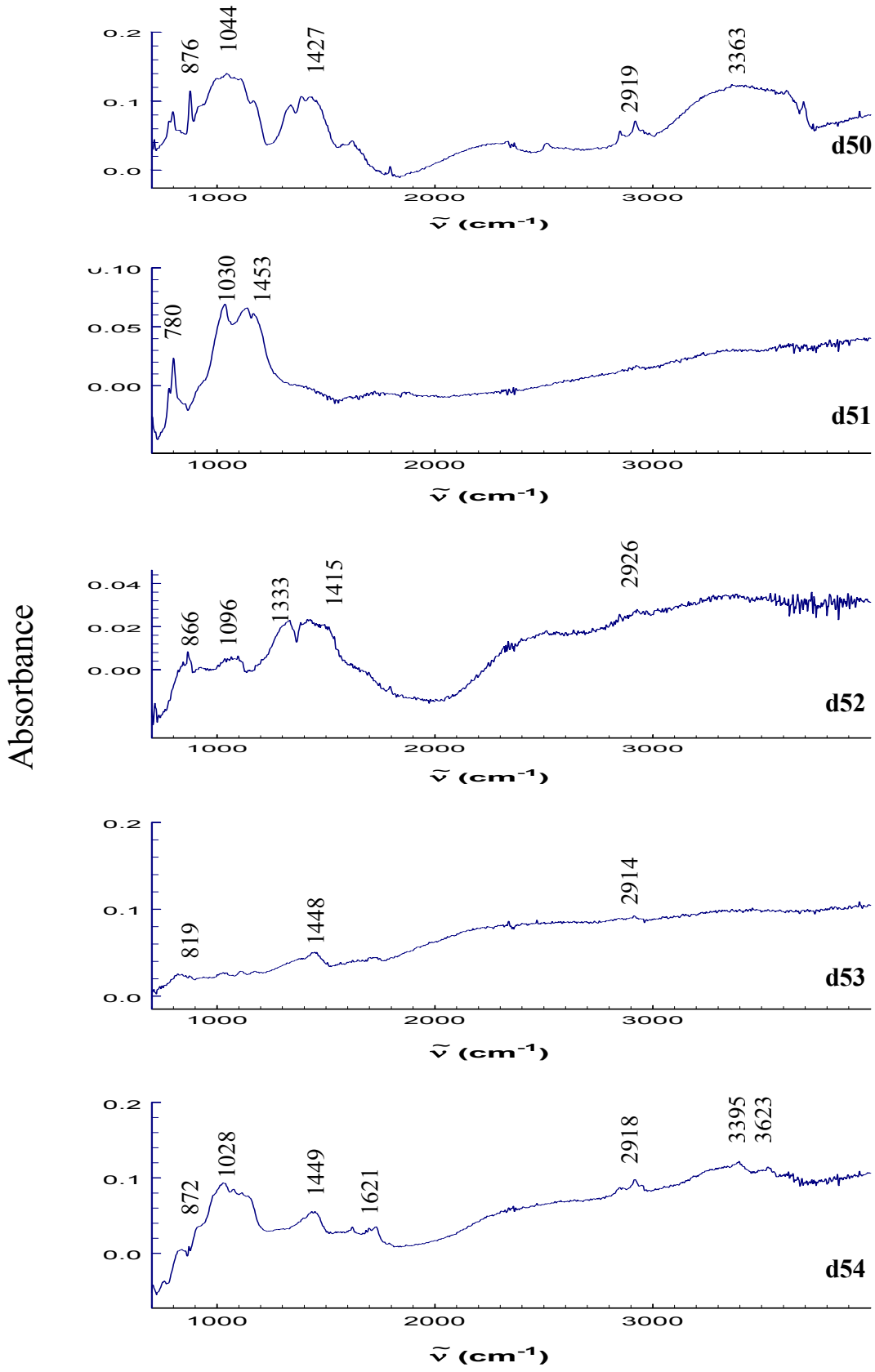

Figure 3.4.11: IR spectra of dust particles d 50, 51, 52, 53, 54.

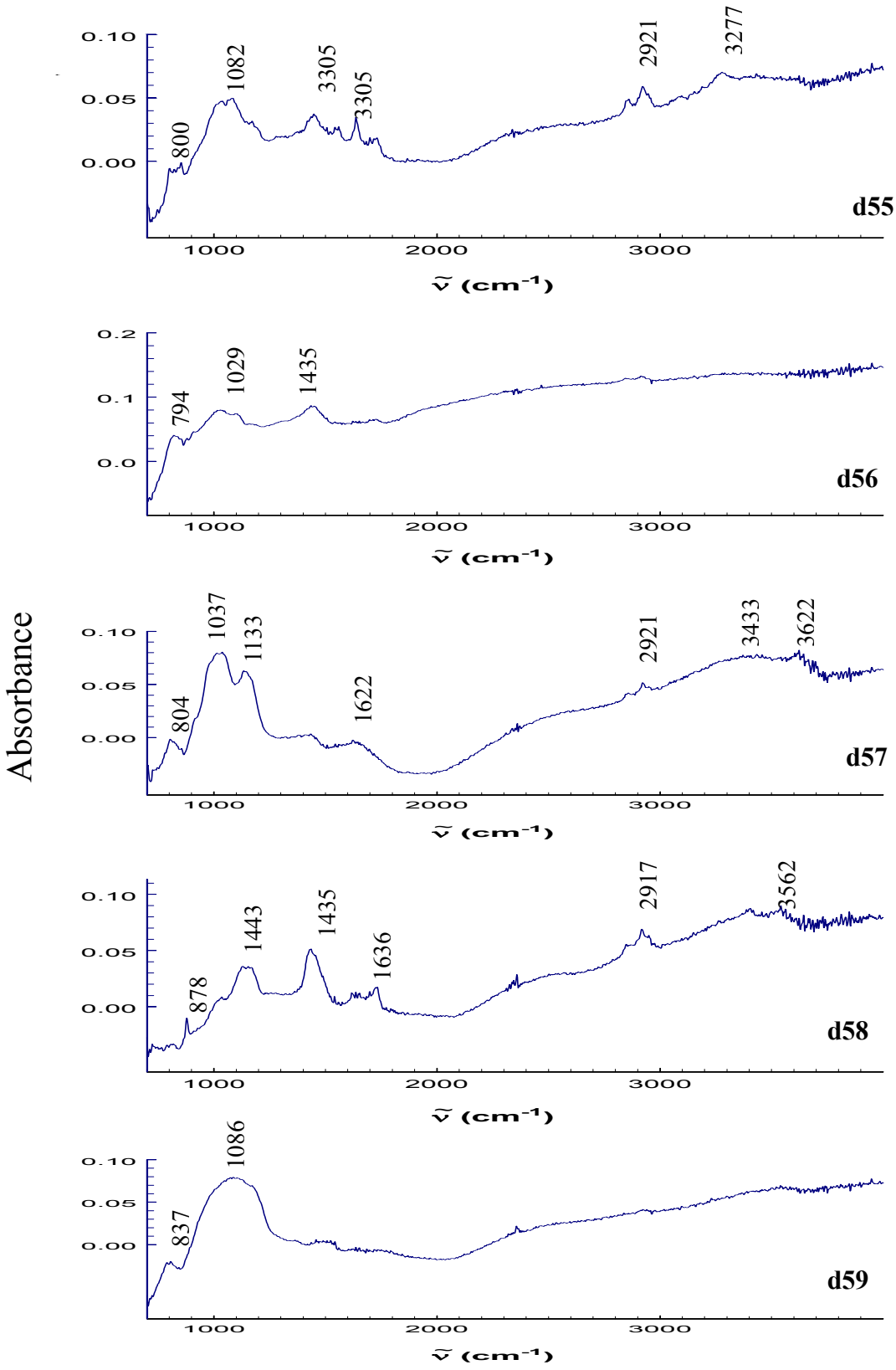

Figure 3.4.12: IR spectra of dust particles d 55, 56, 57, 58, 59.

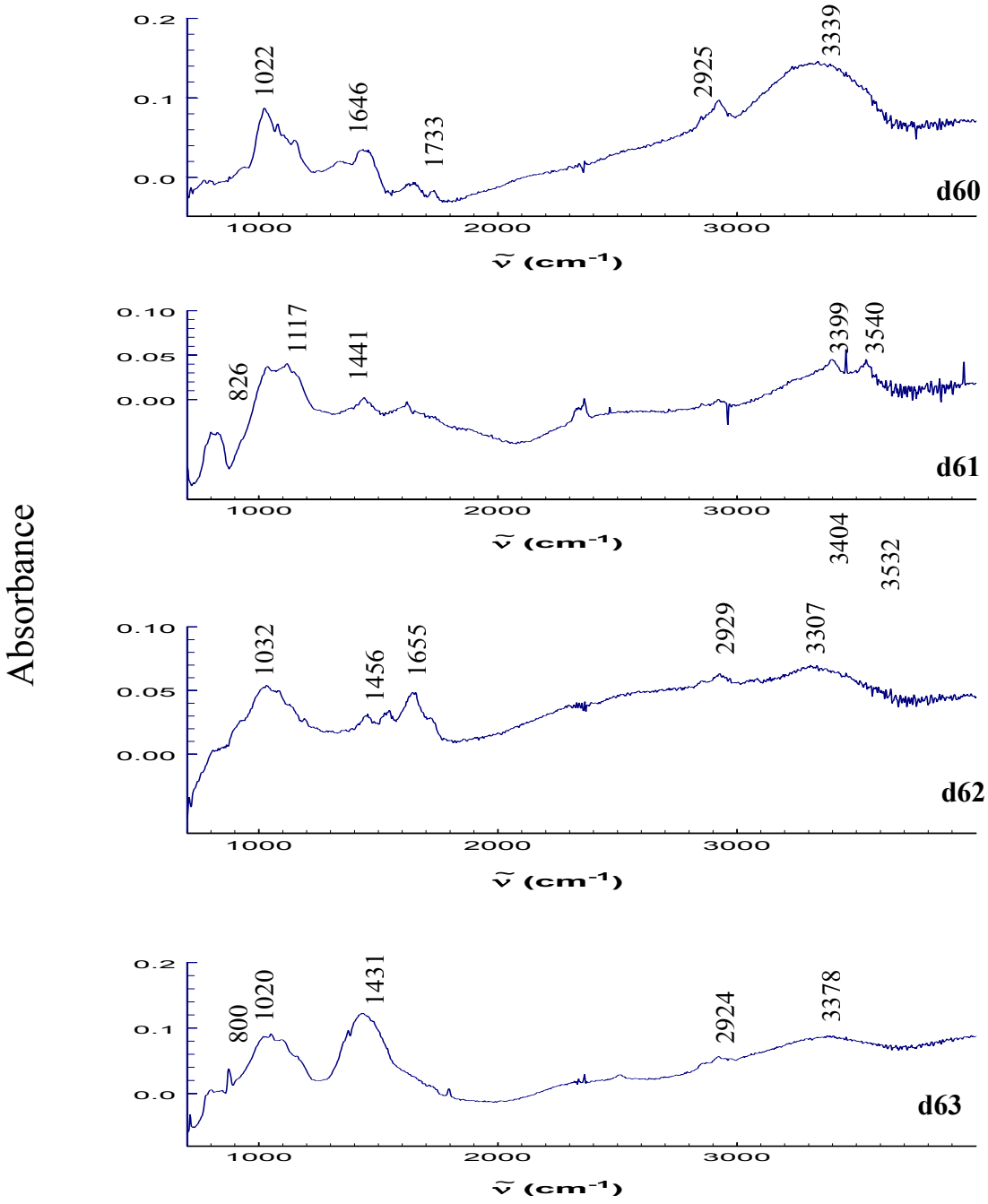

Figure 3.4.13: IR spectra of dust particles d 60, 61, 62, 63.

3.5 Dust Model Calibration

Besides a couple of very interesting and complex spectra, most of the 63 individual particles contain only a handful of common components. Below is a table showing each of the calibration components and some common sources of the material.

Calibration Component	Formula	Source(s)
Calcite	$CaCO_3$	Limestone, Marine Species, Shells
Dolomite	$CaMg(CO_3)_2$	Sedimentary Rock, Mountains
Gypsum	$CaSO_4$	Sedimentary Rock, Drywall
Quartz	SiO_2	Sand, Sandstone, Shale
Kaolinite	$Al_2Si_2O_5(OH)_4$	China Clay, White Clay

Table 3.5: Table of calibration component information.

Other components that will be included in the calibration but could not due to time constraints are Montmorillonite, $(Na,Ca)_{0.33}(Al,Mg)_2(Si_4O_{10})(OH)_2{\cdot}nH_2O$, and Illite, $(K,H_3O)(Al,Mg,Fe)_2(Si,Al)_4O_{10}[(OH)_2,(H_2O)]$, which are the most common clays with with Kaolinite, both sodium nitrate, $NaNO_3$, and ammonium nitrate, NH_4NO_3, Hematite, Fe_2O_3 or rust, and ZnO. The spectra of the five finished calibration components are shown below. In Figures 3.5.1 and 3.5.2, the red curves are the resulting spectra obtained by placing the material in mesh, and are averages of single particle spectra for each component. Blue curves are the ATR spectra of each of the calibrants.

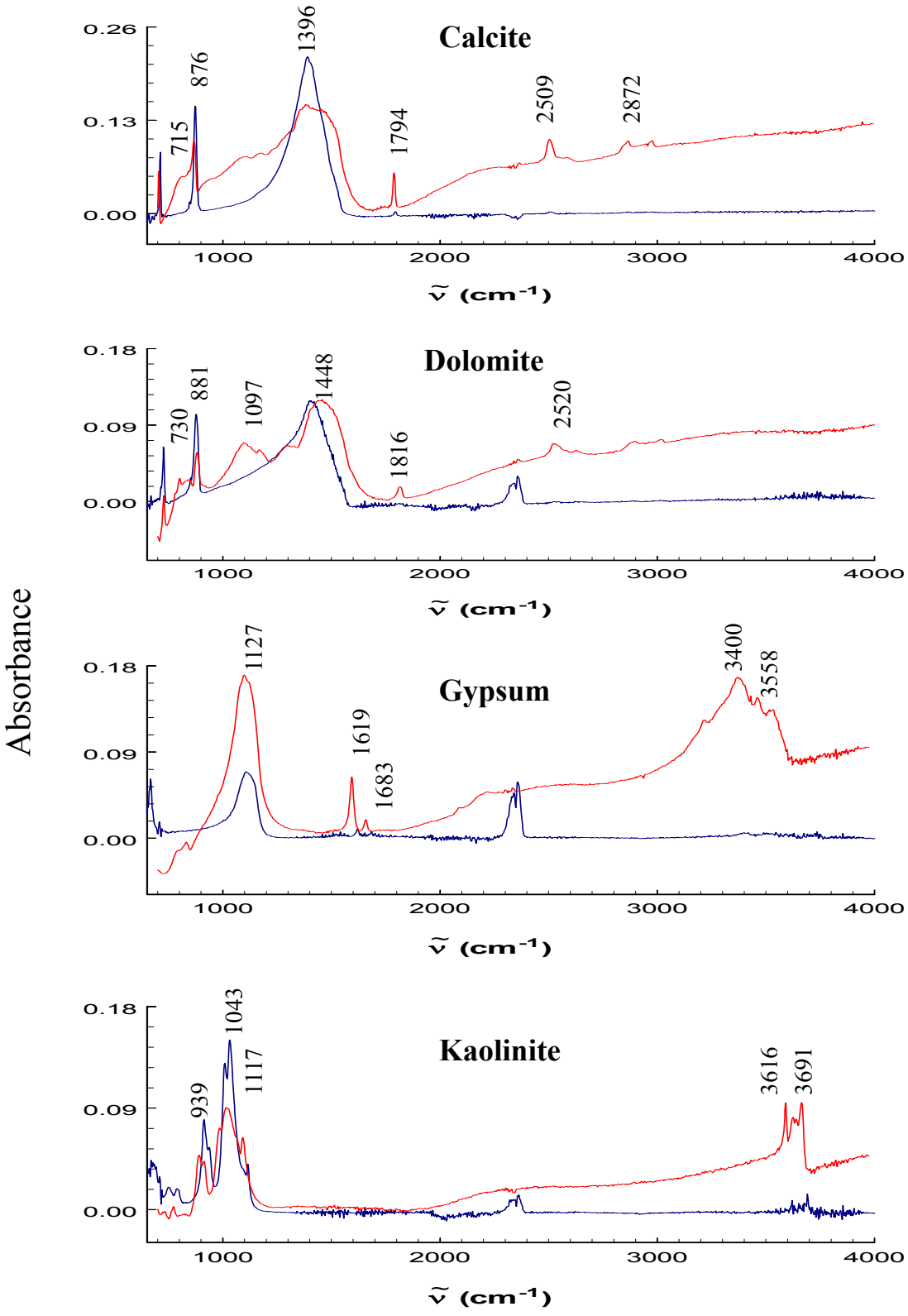

Figure 3.5.1: Red curves are spectra obtained from mesh. Blue curves are ATR spectra.

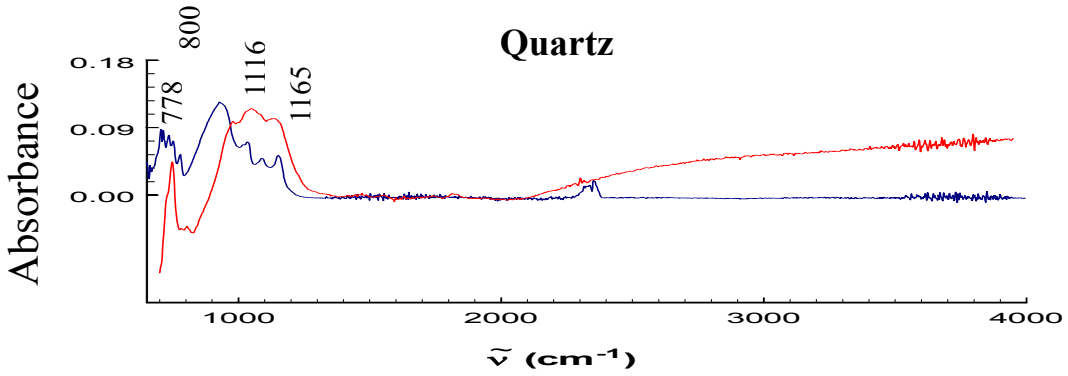

Figure 3.5.2: Red curve is spectra of quartz obtained from mesh. Blue curve is the ATR spectra of quartz.

ATR spectra were taken with the same range of 700-4000 cm^{-1}, 4 cm^{-1} resolution, and 512 scans/pixel. A diamond ATR crystal is brought down on a small amount of the sample on a ZnSe window, and light is then reflected internally through the crystal where the evanescent wave extends into the sample. This beam is then collected by the detector. By using the total internal reflection property of the crystal, no scattered light makes it to the detector, and a pure absorption spectrum is obtained.

There are some obvious differences between the ATR spectra and the spectra obtained from mesh. The vibrations occur at the same position; however the spectra obtained from mesh have extra features, which could be due to a couple factors. First is the baseline. ATR spectra have a flat base line, while the spectra from mesh have a rising baseline due perhaps to generic absorption. Generic absorption arises from the imaginary part of the index of refraction. Overtone vibrations are almost not visible at all in the ATR spectra while they are orders of magnitude more intense in the mesh spectra. The mesh spectra, while some peaks are very narrow, others such as Calcite's vibration at 1435 cm^{-1} are broad and contain, what we believe to be, surface state features based on the shape of

the particle.

More important than shape, is the effect of orientation on the spectra. Due to the small size of the particles, the components are often single crystals and thus all of the components contained in the calibration are either bi/tri-refringent, meaning that once the light enters the sample it is then decomposed into separate rays. In the case of birefringence the light is split into ordinary and extraordinary rays, and in tri-refringent species there are three components to the decomposed light, namely e||a, e||b, and e||c. The difference in the index of refraction for a birefringent material is,

$$\Delta n = n_e - n_o \qquad (3.4).$$

Calcite and hematite are among the most birefringent species, and each ray has its own characteristic spectra containing some of the vibrational components of the average spectra. Depending on the orientation, some vibrations will be more or less intense depending on the contribution from each ray to the overall spectra. This phenomenon was accounted for in the Quartz calibration, as shown by Figure 3.5, but more data is needed for the other materials to adjust for this. By including contributions from factors like surface shape, size, and orientation, the accuracy of the calibration and the theoretical modeling of dust particles will greatly be improved.

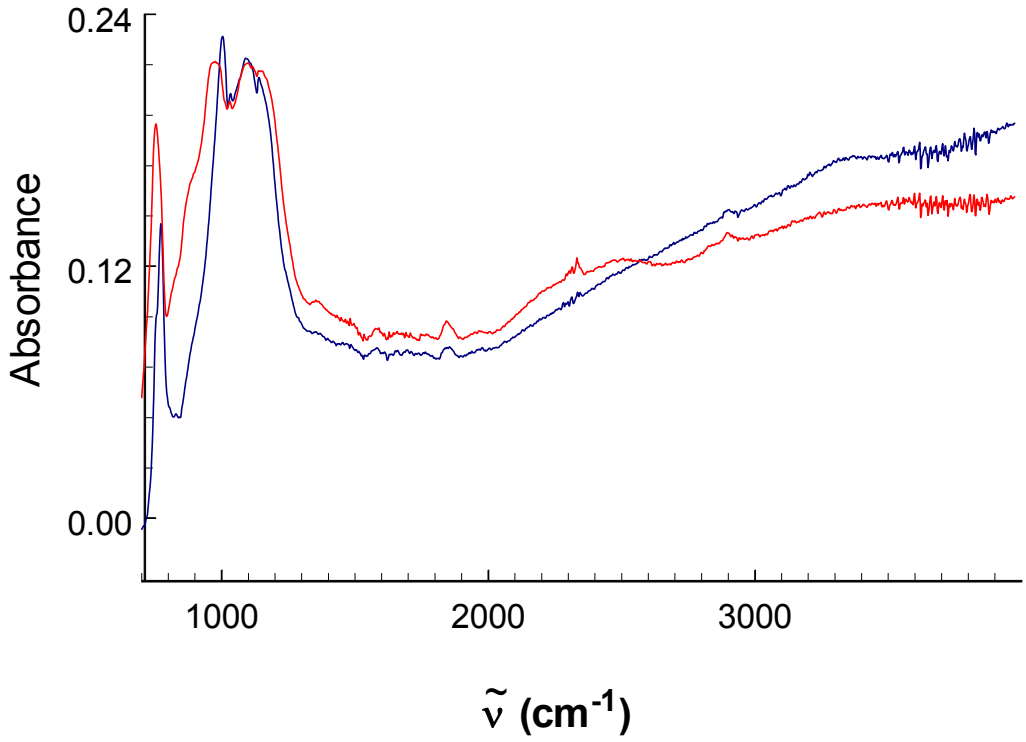

Figure 3.5.3: Red curve is the spectrum of quartz that is dominated by the ordinary ray. Blue curve is of an extraordinary ray dominated spectrum. The ordinary ray of quartz contains the vibration at 778 cm^{-1}, while the extraordinary ray contains the vibration at 800 cm^{-1}. These were obtained through the averaging of multiple particles of quartz, that were separated based on which peak was more intense.

CHAPTER 4
ANALYSIS OF INDIVIDUAL DUST PARTICLES

4.1 Histogram of Peak Positions and Fractional Occurrence of Components

The overall composition of the dust sample can be inspected by simply creating a histogram of all of the peaks contained in all the spectra. Without doing a whole lot of work, a sense of the distribution of components in the spectra can be identified.

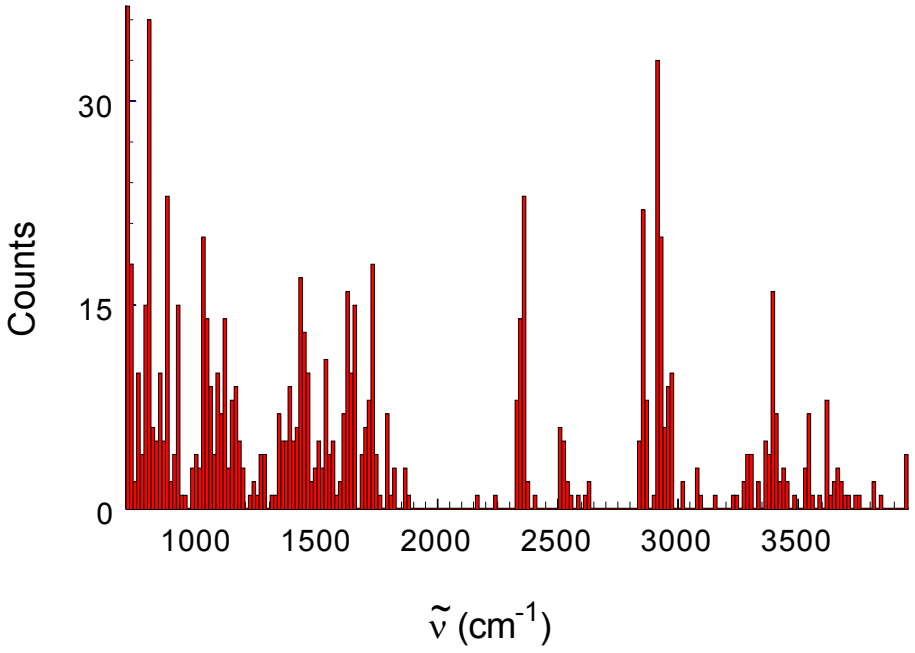

Figure 4.1: Histogram of peak positions contained in the 63 particle spectra.

Table 4.1 contains the abundance of the calibration components in the 63 individual particle spectra.

Component	Number of Particles	% of Total	Identifying Peak (cm^{-1})
Calcite	23	36	715
Dolomite	13	21	730
Gypsum	14	22	1127, Overtones
Quartz	35	56	801, 778
Kaolinite	6	10	1038, Overtones
Other Clays	11	18	1030, Overtones
Organics	36	57	2921

Table 4.1: Table of the occurrences of components contained in the individual dust particles.

4.2 Modeling Mesh Spectra: Mie Scattering Theory Modeling of Calibrants

When a particle's size is on the order of the wavelength of light, the particle will scatter light more than is absorbed. In the figure below, the green curve is the extinction of a 5 μm latex sphere while the red curve is of a latex sphere inside a mesh hole. We can see the effects of scattering in the overall broad nature of the extinction curve. The vibrational features are small compared to scattering, and they also appear in the spectrum out-of-phase due to the interaction of the vibrations with the scattered light[11].

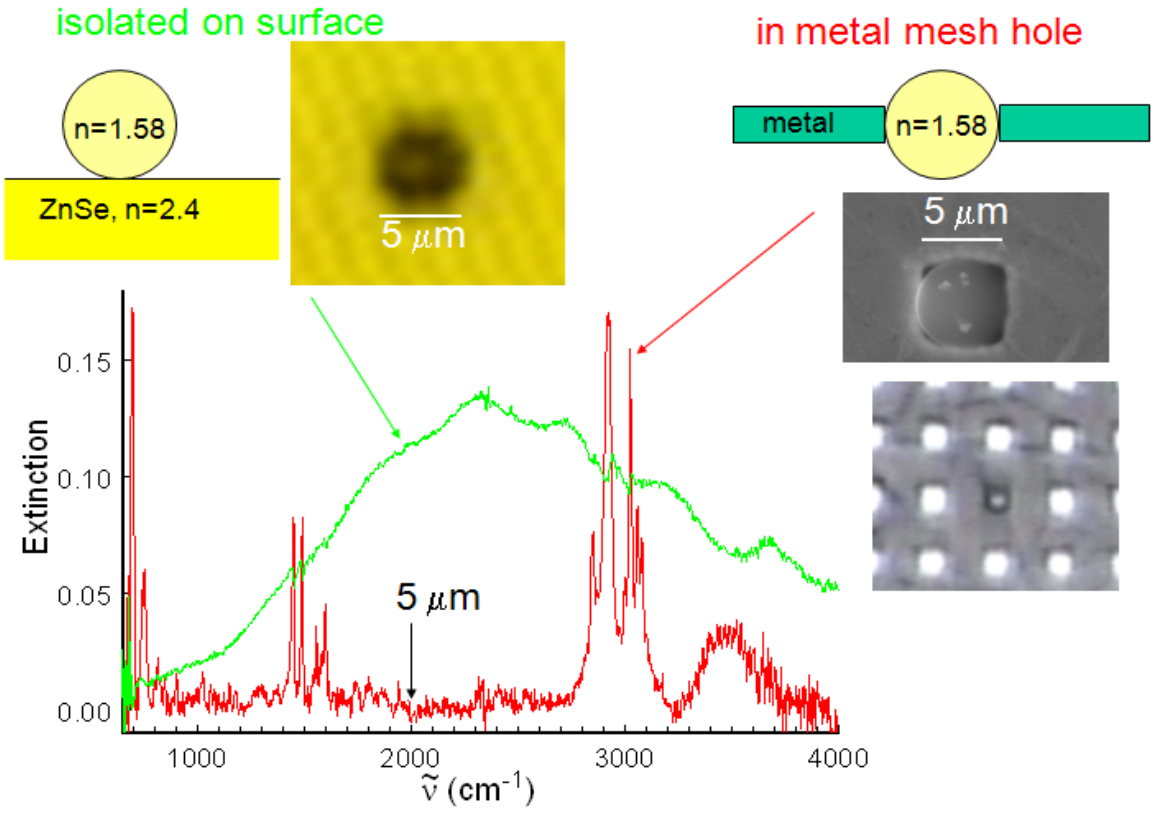

Figure 4.2.1: Green curve is the extinction spectrum of a 5 μm latex sphere on ZnSe. The red curve is a latex sphere in the hole of mesh.

The cross section of extinction, C_{ext}, is the amount of attenuation of the light source due to scattering and absorption[11]. The extinction and scattering cross sections, C_{ext} and C_{sca}, written in terms of the Mie coefficients as,

$$C_{ext} = \frac{1}{2\tilde{\pi}v^2}\sum_{n=1}^{\infty}(2n+1)Re(a_n + b_n) \qquad (4.1),$$

$$C_{sca} = \frac{1}{2\tilde{\pi}v^2}\sum_{n=1}^{\infty}(2n+1)\{|a_n|^2 + |b_n|^2\} \qquad (4.2),$$

$$a_n = \frac{\psi_n'(y)\psi_n(x) - m\psi_n'(x)\psi_n(y)}{\psi_n'(y)\xi_n(x) - m\psi_n(y)\xi_n'(x)} \qquad (4.3),$$

$$b_n = \frac{m\psi_n'(y)\psi_n(x) - \psi_n'(x)\psi_n(y)}{m\psi_n'(y)\xi_n(x) - \psi_n(y)\xi_n'(x)} \qquad (4.4),$$

where $x=2\pi r\tilde{v}$, is the size parameter, r radius of the particle, and a_n and b_n are the Mie coefficients which depend on the complex index of refraction m^*, see equation 4.8. The Mie coefficients involve Riccati-Bessel functions, ψ_n and ξ_n.

$$\xi_n(x) = \left(\frac{\pi x}{2}\right)^{\frac{1}{2}} H^{(2)}_{n+\frac{1}{2}}(x) \qquad (4.5),$$

$$\psi_n(x) = \left(\frac{\pi x}{2}\right)^{\frac{1}{2}} J_{n+1/2}(x) \qquad (4.6),$$

where $J_{n+1/2}$ is the Bessel function of the first kind and $H^{(2)}_{n+1/2}$ is the Hankel function of the second kind.

Once the radius of the particle and the components of the complex index of refraction, n and k, are known or estimated, the extinction and scattering cross sections can be calculated and used to extract the absorbtion cross section,

$$C_{abs} = C_{ext} - C_{sca} \qquad (4.7).$$

To construct a theoretically modeled absorbtion spectrum through Mie Theory, Lorentz vibrational terms must be added to the dielectric constant giving the complex index of refraction as,

$$m^* = \sqrt{\varepsilon} = \sqrt{\varepsilon' + i\varepsilon'' + \sum_j \frac{\tilde{\nu}_{oj}^2 A_j}{\tilde{\nu}_{oj}^2 + \tilde{\nu}^2 + i\gamma\tilde{\nu}}} \qquad (4.8),$$

where A_j is the intensity of each vibration, $\tilde{\nu}_o$ is the position of each peak, and γ is the full width at half max. These parameters are derived from averaged individual spectra obtained from mesh.

There is another small issue when dealing with solid state materials. The dielectric constant, or index of refraction, of components do not add linearly (as in Beer's Law). Each component seems to interact with each other to form an overall effective dielectric constant. This mixing of dielectrics in solid state materials can be described using Bruggeman Effective Medium Theory,

$$\sum_i f_i \frac{\varepsilon_i - \varepsilon_{eff}}{\varepsilon_i + 2\varepsilon_{eff}} = 0 \qquad (4.9),$$

where $\boldsymbol{\varepsilon}_i$ is the dielectric of each material, f_i the fraction of each material, and $\boldsymbol{\varepsilon}_{eff}$ is the effective dielectric for the mixture. However because it is difficult to solve for $\boldsymbol{\varepsilon}_{eff}$, an iterative version of the equation was used (that was derived by Dr. Coe). Starting with Equation 4.9, split the sum into two terms,

$$\sum_{i=0}^{n-1} \frac{f_i \varepsilon_i}{\varepsilon_i + 2\varepsilon_{eff}} - \sum_{i=0}^{n-1} \frac{f_i \varepsilon_{eff}}{\varepsilon_i + 2\varepsilon_{eff}} = 0 \qquad (4.10),$$

$$\sum_{i=0}^{n-1} \frac{f_i \varepsilon_i}{\varepsilon_i + 2\varepsilon_{eff}} = \varepsilon_{eff} \sum_{i=0}^{n-1} \frac{f_i}{\varepsilon_i + 2\varepsilon_{eff}} \quad (4.11),$$

solving for $\boldsymbol{\varepsilon}_{\text{eff}}$,

$$\varepsilon_{eff} = \frac{\sum_{i=0}^{n-1} \frac{f_i \varepsilon_i}{\varepsilon_i + 2\varepsilon_{eff}}}{\sum_{i=0}^{n-1} \frac{f_i}{\varepsilon_i + 2\varepsilon_{eff}}} \quad (4.12).$$

$$\varepsilon_{eff,k} = \frac{\sum_{i=0}^{n-1} \frac{f_i \varepsilon_i}{\varepsilon_i + 2\varepsilon_{eff,k-1}}}{\sum_{i=0}^{n-1} \frac{f_i}{\varepsilon_i + 2\varepsilon_{eff,k-1}}} \quad (4.13)$$

Equation 4.13 is the equation used where f_o,$\boldsymbol{\varepsilon}_o$, and $\boldsymbol{\varepsilon}_{eff\,o}$ are intial guesses. The initial guess, in each case, is the linear combination of each component's fractional amount times the dielectric constant of the material,

$$\varepsilon_{eff_o} = f_0\varepsilon_0 + f_1\varepsilon_1 + \cdots + f_{n-1}\varepsilon_{n-1} = \sum_{i=0}^{n-1} f_i \varepsilon_i \quad (4.14).$$

The resulting simulated spectra, red curves, and each calibrant spectra obtained from mesh, blue curves, are seen below. The Lorentz vibrational parameters are contained in the Mathcad Template, in the Appendix.

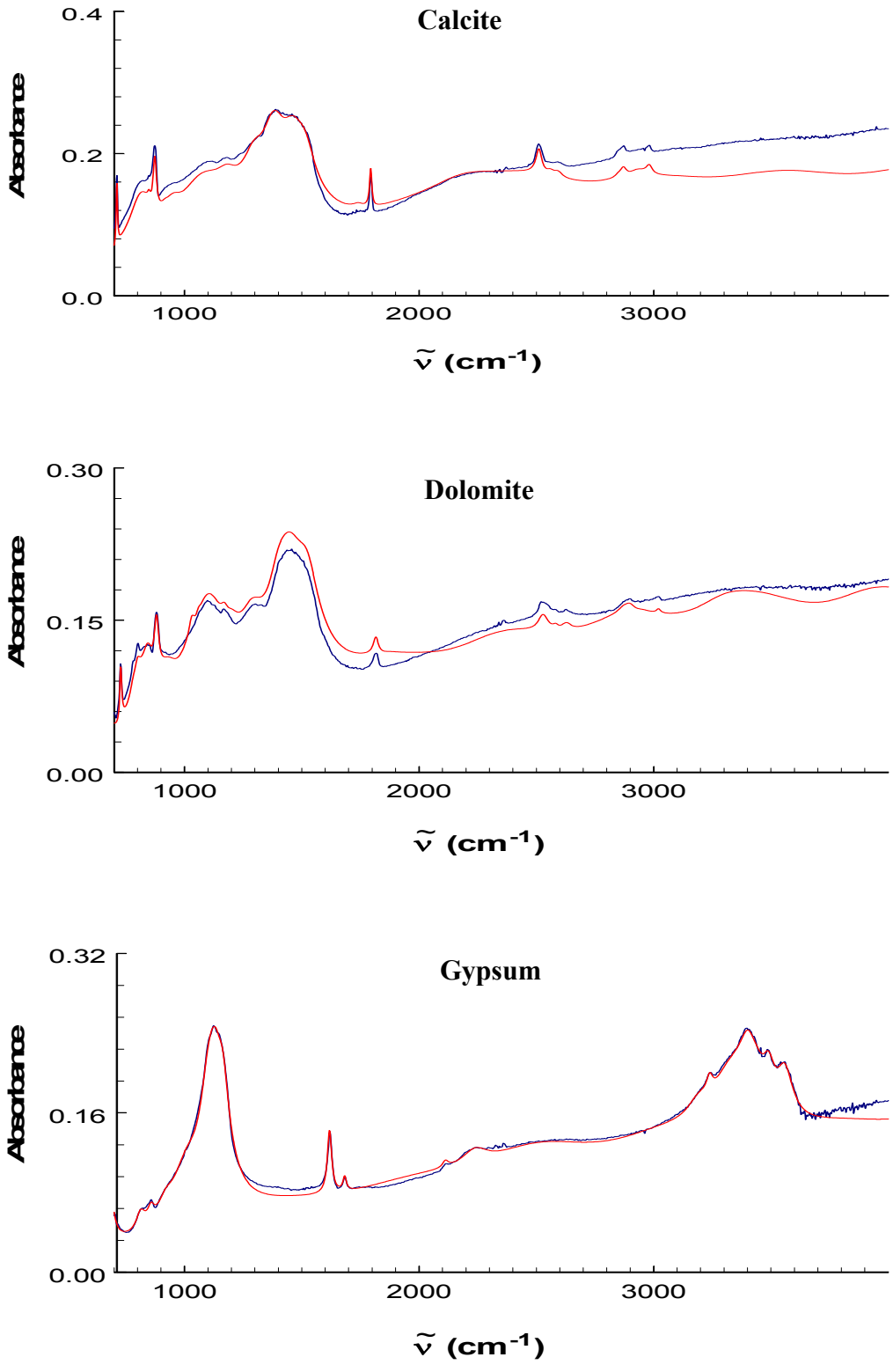

Figure 4.2.2: Blue curves are spectra obtained from mesh. Red curves are the simulated spectra.

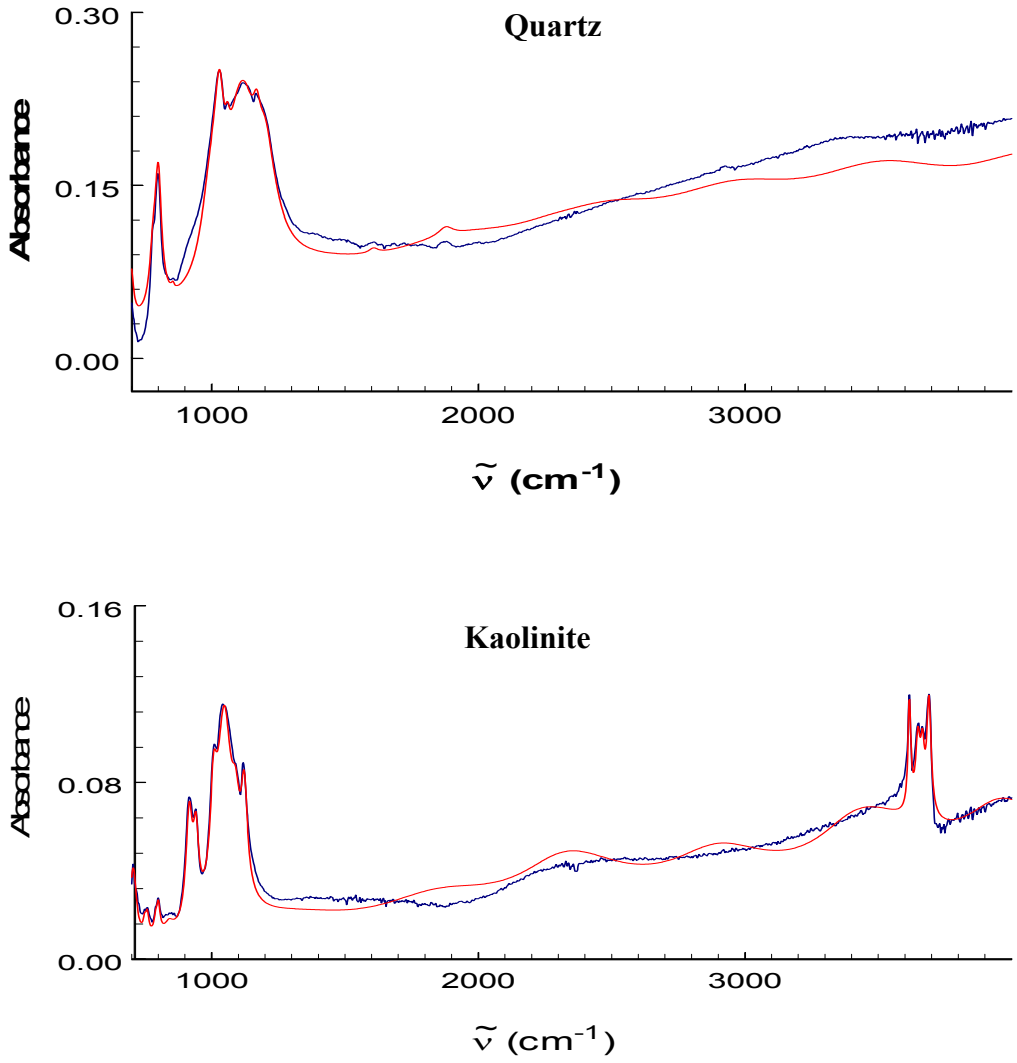

Figure 4.2.3: Blue curves are spectra obtained from mesh. Red curves are the simulated spectra.

4.3 Modeling Individual Dust Spectra

Using the technique described above, the spectra of individual particles can then be simulated to obtain fractional amounts of each calibration component.

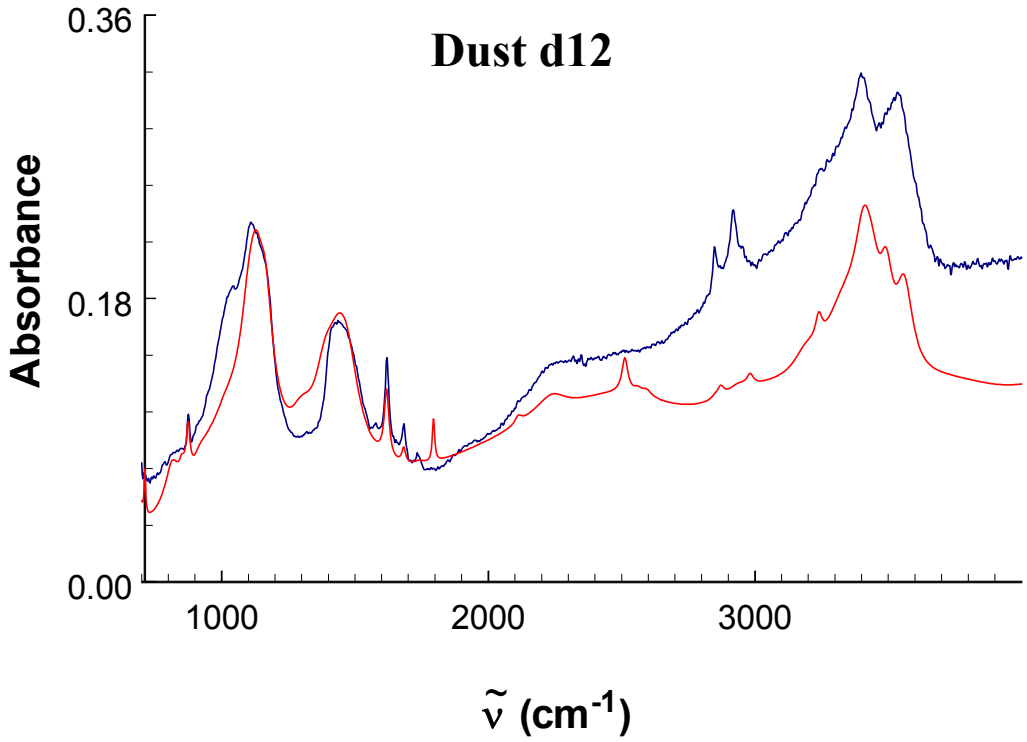

Figure 4.3.1: Blue curve is the spectrum of dust particle d12 and the red curve is the simulated spectrum of d12.

Component	Decimal Fraction
Calcite	0.30
Dolomite	0
Gypsum	0.65
Quartz (ordinary)	0
Quartz (extraordinary)	0
Kaolinite	0
Unknown	0.05

Figure 4.3.1: Table containing the volume fractional amounts of each calibration component contained in dust particle d12.

The fraction parameters are altered until a good fit is obtained. The results from the simulation of dust d12 can be seen in the table above, revealing that is 65% Gypsum, 25% Calcite, and 5% of an unknown material. An unknown material with an average dust dielectric is added to account for materials not in the calibration but still contribute to the volume fraction of the particle.

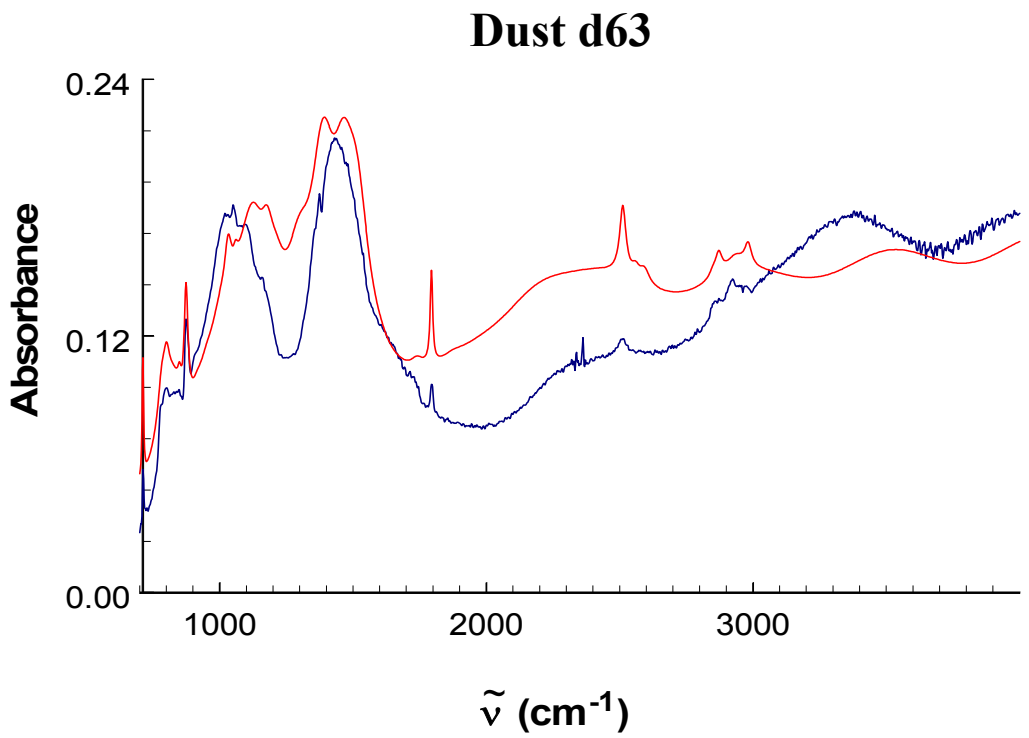

Figure 4.3.2: Blue curve is the spectrum of dust particle d63 and the red curve is the simulated spectrum of d63.

Component	Decimal Fraction
Calcite	0.60
Dolomite	0
Gypsum	0
Quartz (ordinary)	0.07
Quartz (extraordinary)	0.10
Kaolinite	0
Unknown	0.23

Table 4.3.2: Table containing the volume fractional amounts of each calibration component contained in dust particle d63.

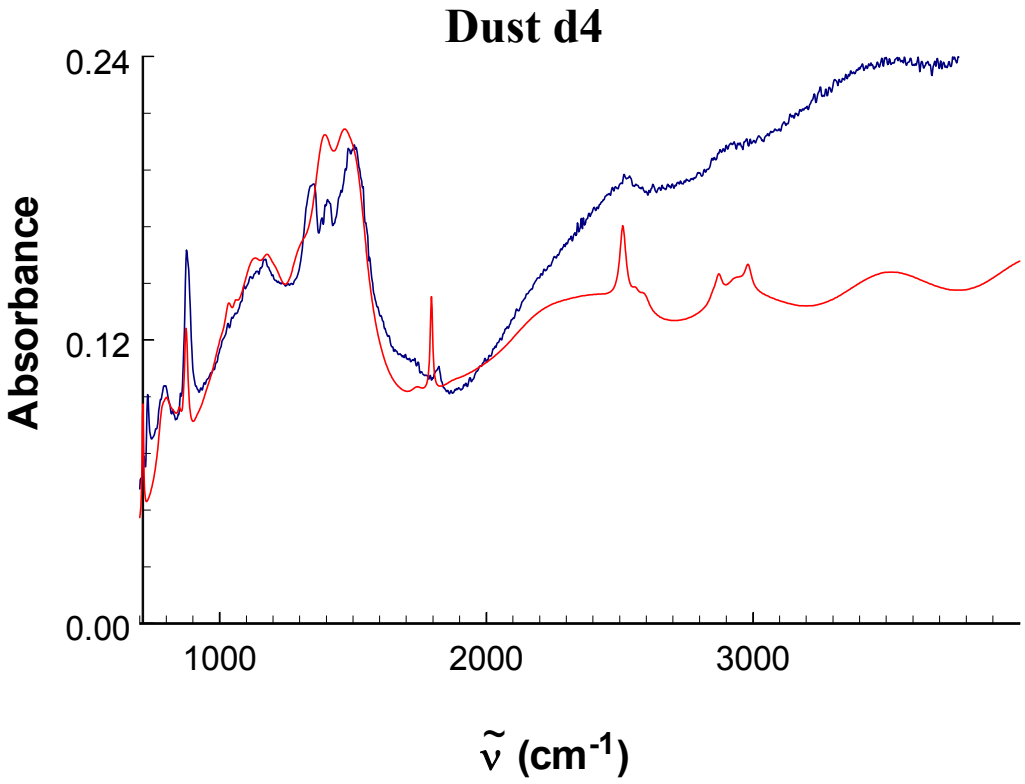

Figure 4.3.3: Blue curve is the spectrum of dust particle d4 and the red curve is the simulated spectrum of d4.

Component	Decimal Fraction
Calcite	0.50
Dolomite	0
Gypsum	0
Quartz (ordinary)	0.07
Quartz (extraordinary)	0.05
Kaolinite	0
Unknown	0.38

Table 4.3.3: Table containing the volume fractional amounts of each calibration component contained in dust particle d4.

CHAPTER 5
CONCLUSION

- The phenomenon of the extraordinary transmission of plasmonic mesh allows for "scatter-free" IR spectra to be taken of individual dust particles.
- The individual particle spectra, for the most part, contain a handful of common components which were included as calibrants. These were calcite, dolomite, gypsum, quartz, and kaolinite.
- With the aid of Mie Scattering Theory and Bruggeman Effective Medium Theory, we can theoretically simulate the individual particle spectra and extract fractional amounts of the calibration components.

WORKS CITED

(1) Boon, K. F.; Kiefert, L.; McTainsh, G. H. *Atmospheric Environment* **1998**, *32*, 2817.

(2) United States Environmental Protection Agency.

(3) Dominici, F., A. McDermott, S.L. Zeger, et al. *Environmental Health Perspectives* **2003**, *111*, 30.

(4) Hong, Y. C.; Pan, X. C.; Kim, S. Y.; Park, K.; Park, E. J.; Jin, X.; Yi, S. M.; Kim, Y. H.; Park, C. H.; Song, S.; Kim, H. *Science of the Total Environment*, *408*, 754.

(5) Oberdörster, J. F., and B E Lehnert. *Environ Health Perspect.* **1994**, *102*, 173–179.

(6) Wolfgang F. Rogge, L. M. H., Monica A. Mazurek, Glen R. Cass, Bernd R. T. Simoneit. *Environmental Science & Technology* **1993**, *27*.

(7) Mohanraj, P. A. A. a. T. P. *Chemistry and Materials Science* **2004**, *47*, 162.

(8) Hoffmann, C.; Funk, R.; Sommer, M.; Li, Y. *Atmospheric Environment* **2008**, *42*, 8422.

(9) Livraghi, A.; Randell, S. H. *Toxicologic Pathology* **2007**, *35*, 116.

(10) Cilwa, K. E.; Rodriguez, K. R.; Heer, J. M.; Malone, M. A.; Corwin, L. D.; Coe, J. V. *The Journal of Chemical Physics* **2009**, *131*, 061101.

(11) Van De Hulst, H. C. **1961**.

APPENDIX A

Mie Theory for Sphere of Arbitrary Size

$$\psi n(n,x) := \left(\frac{\pi \cdot x}{2}\right)^{\frac{1}{2}} \cdot Jn\left(n + \frac{1}{2}, x\right)$$

see p. 123 Van de Hulst

Jn is the mth (n+1/2 in this case) order Bessel function of the first kind.

$$\zeta n(n,x) := \left(\frac{\pi \cdot x}{2}\right)^{\frac{1}{2}} \cdot H2\left(n + \frac{1}{2}, x\right)$$

H2 is the Hankel function of the second kind

$$An(n,x) := \frac{d}{dx}\psi n(n,x) \qquad Bn(n,x) := \frac{d}{dx}\zeta n(n,x)$$

Derivatives of the Bessel and Hankel functions

$r := 2.30 \cdot 10^{-4}$ Radius of particle in units of cm (a parameter in van de Hulst)

set up the wavenumber variable

$imax := 1651 \qquad i := 0 .. imax - 1 \qquad \nu_i := \frac{-i}{imax} \cdot 3302 + 4000 \qquad x2_i := 2 \cdot \pi \cdot r \cdot \nu_i$

Set Volume Fractions

quartz ex	quartz or	calcite	dolomite	gypsum	kaolinite	unknown
$f_0 := 0.05$	$f_1 := 0.07$	$f_2 := .50$	$f_3 := 0.0$	$f_4 := 0.00$	$f_5 := 0.00$	$f_6 := 0.38$

check $f_0 + f_1 + f_2 + f_3 + f_4 + f_5 + f_6 = 1$

quartz extraordinary $\varepsilon 0real := 2.19 \qquad \varepsilon 0imag := .18$

$$\sqrt{\frac{\varepsilon 0real + \sqrt{\varepsilon 0real^2 + \varepsilon 0imag^2}}{2}} = 1.481 \qquad \sqrt{\frac{-\varepsilon 0real + \sqrt{\varepsilon 0real^2 + \varepsilon 0imag^2}}{2}} = 0.061$$

$j0max := 9 \qquad j0 := 0 .. j0max - 1$

$A0_{j0} :=$	$\gamma 0_{j0} :=$	$\nu 00_{j0} :=$
.013	20	697
.035	25	799
0.0006	14	854
.065	30	1030
0.0075	20	1060
.19	100	1112
.025	45	1175
.0003	40	1608
.0006	60	1881

$$\varepsilon 0_i := \varepsilon 0real + i \cdot \varepsilon 0imag + \sum_{j0} \frac{A0_{j0} \cdot (\nu 00_{j0})^2}{(\nu 00_{j0})^2 - (\nu_i)^2 - i \cdot \gamma 0_{j0} \cdot \nu_i}$$

quartz ordinary $\varepsilon 1real := 2.19 \qquad \varepsilon 1imag := .18$

$$\sqrt{\frac{\varepsilon 1real + \sqrt{\varepsilon 1real^2 + \varepsilon 1imag^2}}{2}} = 1.481 \qquad \sqrt{\frac{-\varepsilon 1real + \sqrt{\varepsilon 1real^2 + \varepsilon 1imag^2}}{2}} = 0.061$$

$j1max := 7 \qquad j1 := 0 .. j1max - 1$

$A1_{j1} :=$	$\gamma 1_{j1} :=$	$\nu 01_{j1} :=$
0.060	30	780
0.090	70	995
0.0035	20	1057
.065	90	1130
.050	70	1210
.0003	40	1604
.0006	60	1871

$$\varepsilon 1_i := \varepsilon 1real + i \cdot \varepsilon 1imag + \sum_{j1} \frac{A1_{j1} \cdot (\nu 01_{j1})^2}{(\nu 01_{j1})^2 - (\nu_i)^2 - i \cdot \gamma 1_{j1} \cdot \nu_i}$$

calcite powder $\varepsilon 2real := 2.19$ $\varepsilon 2imag := .18$ $\sqrt{\frac{\varepsilon 2real + \sqrt{\varepsilon 2real^2 + \varepsilon 2imag^2}}{2}} = 1.481$ $\sqrt{\frac{-\varepsilon 2real + \sqrt{\varepsilon 2real^2 + \varepsilon 2imag^2}}{2}} = 0.061$

$j2max := 26$ $j2 := 0..j2max - 1$ $A2_{j2} :=$ $\gamma 2_{j2} :=$ $\nu 02_{j2} :=$

$A2_{j2}$	$\gamma 2_{j2}$	$\nu 02_{j2}$
.007	6	711
.024	140	735
.080	120	815
.001	13	848
0.010	15	874
.0020	40	915
.015	90	950
.090	240	1083
.013	100	1184
.033	110	1300
.065	90	1388
0.047	90	1465
.026	85	1510
0.0005	50	1740
0.0012	10	1794
0.02	400	2200
0.015	500	2440
0.0018	27	2512
0.0003	35	2560
0.0005	45	2593
0.00010	30	2850
0.0004	30	2871.8
0.0009	90	2935
0.0004	30	2982.1
.004	600	3000
.003	600	3433

$$\varepsilon 2_i := \varepsilon 2real + i \cdot \varepsilon 2imag + \sum_{j2} \frac{A2_{j2} \cdot (\nu 02_{j2})^2}{(\nu 02_{j2})^2 - (\nu_i)^2 - i \cdot \gamma 2_{j2} \cdot \nu_i}$$

dolomite $\varepsilon 3real := 1.5^2$ $\varepsilon 3imag := .18$ $\sqrt{\frac{\varepsilon 3real + \sqrt{\varepsilon 3real^2 + \varepsilon 3imag^2}}{2}} = 1.501$ $\sqrt{\frac{-\varepsilon 3real + \sqrt{\varepsilon 3real^2 + \varepsilon 3imag^2}}{2}} = 0.06$

$j3max := 21$ $j3 := 0..j3max - 1$ $A3_{j3} :=$ $\gamma 3_{j3} :=$ $\nu 03_{j3} :=$

$A3_{j3}$	$\gamma 3_{j3}$	$\nu 03_{j3}$
0.0065	10	728.5
.060	130	825
.007	40	843
0.0095	21	881.3
.018	100	930
.037	120	1090
.005	90	1167
0.024	120	1290
.017	90	1404
0.067	125	1452
.028	95	1520
0.0008	26	1816
.002	400	2370
0.0009	50	2529
0.00009	25	2582
0.00033	50	2628
.0002	50	2870
0.00035	50	2897
0.00008	60	2954
0.00007	20	3020

$$\varepsilon 3_i := \varepsilon 3real + i\cdot\varepsilon 3imag + \sum_{j3} \frac{A3_{j3}\cdot\left(\nu 03_{j3}\right)^2}{\left(\nu 03_{j3}\right)^2 - \left(\nu_i\right)^2 - i\cdot\gamma 3_{j3}\cdot\nu_i}$$

gypsum $\varepsilon 4real := 1.975$ $\varepsilon 4imag := .15\cdot 0.5$ $\sqrt{\frac{\varepsilon 4real + \sqrt{\varepsilon 4real^2 + \varepsilon 4imag^2}}{2}} = 1.406$ $\sqrt{\frac{-\varepsilon 4real + \sqrt{\varepsilon 4real^2 + \varepsilon 4imag^2}}{2}} = 0.027$

$j4max := 19$ $j4 := 0..j4max - 1$

$A4_{j4} :=$	$\gamma 4_{j4} :=$	$\nu 04_{j4} :=$
.075	13.6	667
.0055	45	813
.0030	35	857
.006	75	920
.033	150	1010
.0066	50	1103
.078	75	1127
.015	47	1163
0.0025	20	1618.7
0.00040	18	1683
.00021	30	2113
.0020	130	2240
0.006	530	2520
0.0015	110	3192
0.00054	30	3240
0.0070	170	3335
0.014	50	3423
0.0035	45	3493
0.0035	60	3560

$$\varepsilon 4_i := \varepsilon 4real + i\cdot\varepsilon 4imag + \sum_{j4} \frac{A4_{j4}\cdot\left(\nu 04_{j4}\right)^2}{\left(\nu 04_{j4}\right)^2 - \left(\nu_i\right)^2 - i\cdot\gamma 4_{j4}\cdot\nu_i}$$

kaolinite powder $\varepsilon 5real := 1.5^2$ $\varepsilon 5imag := .18$ $\sqrt{\frac{\varepsilon 5real + \sqrt{\varepsilon 5real^2 + \varepsilon 5imag^2}}{2}} = 1.501$ $\sqrt{\frac{-\varepsilon 5real + \sqrt{\varepsilon 5real^2 + \varepsilon 5imag^2}}{2}} = 0.06$

$j5max := 19$ $j5 := 0..j5max - 1$

$A5_{j5} :=$	$\gamma 5_{j5} :=$	$\nu 05_{j5} :=$
.0085	28	705
.00060	13	749
.00083	13	759
.0006	15	790
.0012	15	800
.001	40	840
.0066	28	916
.0037	24	941
.0050	30	1008
.020	60	1048
.0033	35	1090
0.0039	28	1122
.002	400	2300
0.0	300	2924
0.0011	500	3600
0.00019	13	3617
0.00018	20	3649
0.00012	17	3666
0.00027	18	3690

$$\varepsilon 5_i := \varepsilon 5real + i\cdot\varepsilon 5imag + \sum_{j5} \frac{A5_{j5}\cdot\left(\nu 05_{j5}\right)^2}{\left(\nu 05_{j5}\right)^2 - \left(\nu_i\right)^2 - i\cdot\gamma 5_{j5}\cdot\nu_i}$$

unknown $\varepsilon 6real := 1.5^2$ $\varepsilon 6imag := .18$ $\varepsilon 6real := 2.34$ $\varepsilon 6imag := .04$

$$\sqrt{\frac{\varepsilon 6real + \sqrt{\varepsilon 6real^2 + \varepsilon 6imag^2}}{2}} = 1.53 \qquad \sqrt{\frac{-\varepsilon 6real + \sqrt{\varepsilon 6real^2 + \varepsilon 6imag^2}}{2}} = 0.013$$

$\varepsilon 6_i := \varepsilon 6real + i \cdot \varepsilon 6imag$

Bruggeman Effective Medium Theory

number of iterations $k := 1..10$

first guess $\varepsilon f_{i,0} := f_0 \cdot \varepsilon 0_i + f_1 \cdot \varepsilon 1_i + f_2 \cdot \varepsilon 2_i + f_3 \cdot \varepsilon 3_i + f_4 \cdot \varepsilon 4_i + f_5 \cdot \varepsilon 5_i + f_6 \cdot \varepsilon 6_i$

Iterative Formula

$$\varepsilon f_{i,k} := \frac{\frac{f_0 \cdot \varepsilon 0_i}{\varepsilon 0_i + 2 \cdot \varepsilon f_{i,k-1}} + \frac{f_1 \cdot \varepsilon 1_i}{\varepsilon 1_i + 2 \cdot \varepsilon f_{i,k-1}} + \frac{f_2 \cdot \varepsilon 2_i}{\varepsilon 2_i + 2 \cdot \varepsilon f_{i,k-1}} + \frac{f_3 \cdot \varepsilon 3_i}{\varepsilon 3_i + 2 \cdot \varepsilon f_{i,k-1}} + \frac{f_4 \cdot \varepsilon 4_i}{\varepsilon 4_i + 2 \cdot \varepsilon f_{i,k-1}} + \frac{f_5 \cdot \varepsilon 5_i}{\varepsilon 5_i + 2 \cdot \varepsilon f_{i,k-1}} + \frac{f_6 \cdot \varepsilon 6_i}{\varepsilon 6_i + 2 \cdot \varepsilon f_{i,k-1}}}{\frac{f_0}{\varepsilon 0_i + 2 \cdot \varepsilon f_{i,k-1}} + \frac{f_1}{\varepsilon 1_i + 2 \cdot \varepsilon f_{i,k-1}} + \frac{f_2}{\varepsilon 2_i + 2 \cdot \varepsilon f_{i,k-1}} + \frac{f_3}{\varepsilon 3_i + 2 \cdot \varepsilon f_{i,k-1}} + \frac{f_4}{\varepsilon 4_i + 2 \cdot \varepsilon f_{i,k-1}} + \frac{f_5}{\varepsilon 5_i + 2 \cdot \varepsilon f_{i,k-1}} + \frac{f_6}{\varepsilon 6_i + 2 \cdot \varepsilon f_{i,k-1}}}$$

index of refraction from dielectric $ms_i := \sqrt{\varepsilon f_{i,10}}$ $m_i := \overline{ms_i}$ the imaginary generic part must be negative for the Mie theory

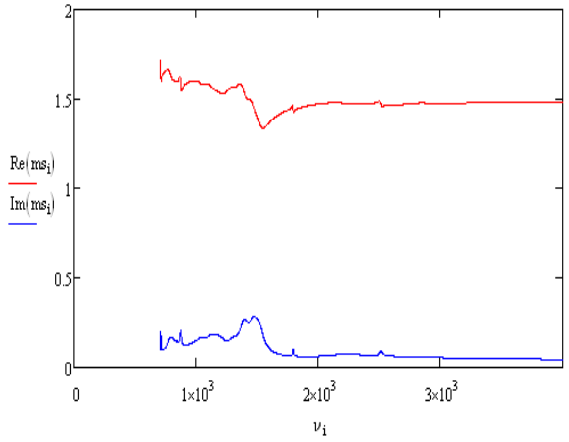

see p. 192 Van de Hulst, except that we have generic absorption and more than one vibration

now calculated as an array because the index of refraction is no longer a constant, it varies when close to a vibration

Mie coefficients $s := 1..20$

$$a_{s,i} := \frac{\psi n(s, x2_i) \cdot An(s, m_i \cdot x2_i) - m_i \cdot An(s, x2_i) \cdot \psi n(s, m_i \cdot x2_i)}{\zeta n(s, x2_i) \cdot An(s, m_i \cdot x2_i) - m_i \cdot Bn(s, x2_i) \cdot \psi n(s, m_i \cdot x2_i)}$$

see p. 123 Van de Hulst

$$b_{s,i} := \frac{\psi n(s, x2_i) \cdot m_i \cdot An(s, m_i \cdot x2_i) - An(s, x2_i) \cdot \psi n(s, m_i \cdot x2_i)}{\zeta n(s, x2_i) \cdot m_i \cdot An(s, m_i \cdot x2_i) - Bn(s, x2_i) \cdot \psi n(s, m_i \cdot x2_i)}$$

this scaling factor is in terms of the spherical value $\alpha := \pi \cdot r^2 \cdot 1.00$ $\alpha = 1.662 \times 10^{-7}$

$$Qa_i := \left[\frac{2}{(x2_i)^2} \cdot \sum_{s=1}^{20} \left[(2 \cdot s + 1) \cdot \left[Re\left(a_{s,i} + b_{s,i}\right) - \left[\left(|a_{s,i}| \right)^2 + \left(|b_{s,i}| \right)^2 \right] \right] \right] \right]$$

Absorption

$$Qe_i := \left[\frac{2}{(x2_i)^2} \cdot \sum_{s=1}^{20} \left[(2 \cdot s + 1) \cdot \left(Re\left(a_{s,i} + b_{s,i}\right) \right) \right] \right]$$

convert to absolute cross sections $Ca_i := \alpha \cdot Qa_i$ $Ce_i := \alpha \cdot Qe_i$

$Csim_i := Ca_i$

input the experimental absorption spectrum

$g := READPRN("d4\_abs.txt")$ $ng := rows(g)$ $ig := 0 .. ng - 1$ $ng = 1.651 \times 10^3$

place on absolute scale $goff := 0.09$ $g_{ig,1} := 9.54 \cdot 10^{-7} \cdot \left(g_{ig,1} + goff \right)$

this calibration value is average of
the yeast and latex sphere results